Eur. Phys. J. B **15**, 765–786 (2000)

THE EUROPEAN
PHYSICAL JOURNAL B
EDP Sciences

A wavelet-based method for multifractal image analysis. III. Applications to high-resolution satellite images of cloud structure

S.G. Roux[1,2], A. Arnéodo[1,a], and N. Decoster[1]

[1] Centre de Recherche Paul Pascal, avenue Schweitzer, 33600 Pessac, France
[2] Climate & Radiation Branch, NASA's Goddard Space Flight Center, Greenbelt, Maryland 20771, USA

Received 17 August 1999

Abstract. We apply the 2D wavelet transform modulus maxima (WTMM) method to high-resolution LANDSAT satellite images of cloudy scenes. The computation of the $\tau(q)$ and $D(h)$ multifractal spectra for both the optical depth and the radiance fields confirms the relevance of the multifractal description to account for the intermittent nature of marine stratocumulus clouds. When assisting the 2D WTMM method by the wavelet based deconvolution method designed to compute the self-similarity kernel, we show that our numerical tools are very efficient to disentangle the anisotropic texture induced by the presence of convective rolls from the background radiance fluctuations which are likely to display isotropic scale invariance. Moreover, this analysis reveals that with the available set of experimental data, there is no way to discriminate between various phenomenological cascade models recently proposed to account for intermittency and their log-normal approximations. When further investigating the "two-point" space-scale correlation functions, we bring definite proof of the existence of an underlying multiplicative structure from an "integral" coarsest scale which is given by the characteristic width of the convective patterns. We emphasize the log-normal random $\mathcal{W}$-cascade model on separable wavelet orthogonal basis introduced in paper II (N. Decoster, S.G. Roux, A. Arnéodo, Eur. Phys. J. B **15**, 739 (2000)), as a very attractive model (at least as compared to the models commonly used in the literature) of the cloud architecture. Finally, we comment on the multifractal properties of marine stratocumulus radiance fields comparatively to previous experimental analysis of velocity and temperature fluctuations in high Reynolds number turbulence.

PACS. 92.60.Nv Cloud physics – 47.27.Jv High-Reynolds-number turbulence – 05.40.+j Fluctuation phenomena, random processes, noise, and Brownian motion – 47.53.+n Fractals

1 Introduction

The problematic of nonlinear variability over a wide range of scales has been considered for a long time with respect to the highly intermittent nature of turbulent flows in fluid dynamics [1–4]. Special attention has been paid to their asymptotic and possibly universal behavior when the dissipation length goes to zero, *i.e.*, when the Reynolds number goes to infinity. Besides wind-tunnel and laboratory (grid, jet, ...) experiments, the atmosphere is a huge natural laboratory where high Reynolds number (fully developed) turbulent dynamics can be studied. Clouds, which are at the source of the hydrological cycle, are the most obvious manifestation of the earth's turbulent atmospheric dynamics [5–8]. By modulating the input of solar radiation, they play a critical role in the maintenance of the earth's climate [9]. They are also one of the main sources of uncertainty in current climate modeling [10], where clouds are assumed to be homogeneous media lying parallel to the earth's surface; at best, a linear combination of cloudy and clear portions according to cloud fraction is used to account for horizontal inhomogeneity when predicting radiative properties. During many years, the lack of data hindered our understanding of cloud microphysics and cloud-radiation interactions. Nowadays, it is well-recognized that clouds are variable in all directions and that fractal [5,6,11–16] and multifractal [7,8,17–19] concepts are likely to be relevant to the description of the complex 3D geometry of clouds. Note that by cloud geometry, we mean not only their external convoluted shapes which are spectacular consequences of the surrounding convection, shear and ensuing turbulence, but also their intermittent internal structure which is likely to have strong impact on radiation transport [8,17,20–25]. Until quite recently, the internal structure of clouds was probed by balloons or aircrafts that penetrated the cloud layer, revealing an extreme variability of 1D cuts of some cloud fields [19,26–33]. In

---

[a] e-mail: `arneodo@crpp.u-bordeaux.fr`

particular, *in situ* measurements of cloud liquid water content (LWC) were performed during many intensive field programs (FIRE [34], ASTEX [35], SOCEX [36] ...). Indeed, during the past fifteen years, vast amounts of data on the distribution of atmospheric liquid water from a variety of sources were collected and analyzed in many different ways. All these data contain information on spatial and/or temporal correlations in cloudiness, enabling the investigation of scale invariance over a range from a few centimeters to hundred of kilometers. An attractive alternative to *in situ* probing is to use high-resolution satellite imagery that now provides direct information about the fluctuations in liquid water concentration in the depths of clouds [12,14–16,21,25,37–41]. These rather sophisticated remote sensing systems called "millimeter radars" are actually sensitive not only to precipating rain drops but also to suspended cloud droplets. Spectral analysis of the recorded 2D radiance field [21,25,37–41] confirms previous 1D findings that make it likely that cloud scenes display scaling over a wide range of scales.

Fractal analysis of atmospheric data has gained considerable momentum since Lovejoy's seminal paper [5] on the area-perimeter relation for clouds and rain. Since then, such morphological studies have become rather popular, following a path open by Mandelbrot in his famous books [42]. Starting from the middle eighties, high-resolution cloud liquid water data became available, confirming the fractal nature of the cloud structure. Most preliminary analysis of these complex 1D signals focused on the characterization of scale invariance in Fourier space [25–32]. In particular, the fluctuations of liquid water density in clouds were shown to have power-law energy spectra, $S(k) \sim 1/k^{\beta}$, over a large range of scales, from tens of meters to tens of kilometers. Let us point out that the estimated spectral exponent $\beta \sim 1.4-1.7$, is close to the prediction $\beta = 5/3$ of Corssin [43]-Obukhov [44] phenomenology for a passive scalar in fully developed 3D turbulence as well as to Kraichnan [45] prediction for 2D turbulence. But as discussed in Section 3.1 of paper I [46], power-spectral analysis has been heavily criticized for its intrinsic inability to capture multifractal scaling. From the measurement of the spectral exponent $\beta = 2H + 1$, one gets some estimate of the so-called Hurst exponent, $H \sim 0.20-0.35$, from which one learns that the fluctuating field is singular and non stationary ($0 < H < 1$). Unfortunately, the intermittent nature of the recorded liquid water data required new concepts and more elaborated technical tools. Again, one has to give credit to Lovejoy and co-workers [17,18,47–54] for applying the multifractal description to atmospheric phenomena. Using the trace moment and double trace moment techniques [49–54], they have brought experimental evidence for multiple scaling (or in other words, the existence of a continuum of scaling exponent values) in various geophysical fields. More recently, Davis and co-workers [8,19,33,41] have used the structure function method to study LWC data recorded during ASTEX and FIRE programs. Both these analyses converge to the conclusion that the internal marine stratocumulus (Sc) structure is multifractal over at least three decades in scales. Quite similar multifractal behavior has been reported by Wiscombe *et al.* [40] when analyzing liquid water path (LWP) data (*i.e.*, column integrated LWC), from the Atmosperic Radiation Measurement (ARM) archive. Even though all these studies seem to agree, at least as far as their common diagnostic of multifractal scaling of the cloud structure, they all concern 1D data. To our knowledge, the structure function method has been also applied to 1D cuts of high-resolution satelitte images [25,55], but we are not aware of any results coming out from a specific 2D analysis.

In this paper, our first goal is to take advantage of the 2D wavelet transform modulus maxima (WTMM) method introduced in paper I [46] and further tested on synthetic multifractal surfaces in paper II [56], to carry out a multifractal analysis of high-resolution satelitte images of Sc cloudy scenes [57,58]. Our objective is not only to extend previous analysis of 1D profiles to full 2D image processing, but also to remedy to the insufficiencies of the structure function method which, as pointed out in references [59–62], fails to achieve complete multifractal characterization. Theoretically, only the strongest singularities, corresponding to the increasing branch of the $D(h)$ singularity spectrum, are amenable to this method. Moreover, there is a risk that the possible existence of very weak ($h > 1$) singularities as well as regular behavior induces some bias in the estimate of the structure function scaling exponents $\tau(q)$ for $q > 0$. As successfully experienced in paper II [56], the application of the 2D WTMM method is likely to provide reliable quantitative estimates of the entire $\tau(q)$ and $D(h)$ multifractal spectra, within the perspective of confirming the intermittent nature of the internal cloud structure. Although this result would not be a surprise in such a highly turbulent environment, the possibility of comparing quantitatively the statistical scaling properties of the optical depth or the radiance fields with those of the velocity or temperature fluctuations in high Reynolds turbulent flows, might be very instructive as far as the influence of atmospheric dynamics on the liquid water distribution in clouds.

Beyond the issue of improving statistical characterization of *in situ* and remotely sensed data, there is a most challenging aspect which consists in extracting structural information to constraint stochastic cloud models which in turn will be used for radiative transfer simulations [8,15,17,20,22,23,25,41,63–66]. Then by comparing the multifractal properties of the numerically generated artificial radiation fields with those of actual measurements, one can hope to achieve some degree of closure. As reviewed in the introduction of paper II [56], in contrast to the proliferation of multiplicative cascade models for the generation of singular measures [47–54,67–78], there exist in the literature, only a few examples of models for generating multifractal functions [61,79–82]. Surprisingly, it is in the context of geophysical data modeling that 1D and 2D synthesis algorithms have been introduced to account for the pioneering observations of multifractal scaling. To bridge the gap between multifractal measures and multifractal functions, Schertzer and Lovejoy in 1987 [49] proposed a straightforward generalization of the devil's staircase concept. As a mean of introducing the continuity that necessarily comes with multi-affine functions, they suggested to use "fractional" integration instead of its standard counterpart. This power-law filtering of singular cascade measures is known as Fractionally Integrated Singular Cascades (FISCs [49–51,54,83]). Another route from multiplicative singular cascades to nonstationary multiscaling processes was charted by Cahalan *et al.* in 1990 [84] for the purpose of modeling the fluctuations of internal structure in marine stratocumulus. The main idea of the so-called "bounded" cascade models, further developed in reference [85], consists in acting on the multiplicative weights during the cascade in physical space to recover continuity in the small-scale limit. One of the major issue addressed in the present work, is to use our algorithmic battery (developed in paper II [56]) to compute the self-similarity kernel and the "space-scale" correlation functions, with the specific goal to reveal the existence of a multiplicative cascade process underlying the spatial fluctuations of both the radiance and the optical depth fields of marine Sc clouds. As the main outcome of this analysis, we will show that the log-normal random $\mathcal{W}$-cascade model introduced in Section 2.2 of paper II [56], provides a very attractive modeling of the internal cloud structure [86] that can be further used to "feed" numerical codes for cloud-radiation studies. Our final message will thus consist in emphasizing the wavelet techniques as rather powerful and very promising tools for statistical cloud data analysis as well as for image synthesis of artificial rough surfaces that statistically reproduce the intermittent nature of real clouds.

The paper is organized as follows. In Section 2, we present the 2D radiance and optical depth data collected by Landsat imagery of marine Sc clouds. We comment on the geophysical importance of analyzing marine Sc. They are one of the most studied cloud types, partly because they exert a systematic effect on the global radiation budget. In Section 3, we use the 2D WTMM method to perform a comparative multifractal analysis of the radiance and optical depth fields. We show that for both fields, the $\tau(q)$ and $D(h)$ multifractal spectra are well approximated by parabolic curves, the signature of log-normal statistics. In Section 4, we apply the wavelet based deconvolution method designed to compute the self-similarity kernel, to radiance LANDSAT images. This method turns out to be very efficient to disentangle the anisotropic texture induced by the presence of convective rolls from the background radiance fluctuations which display nearly isotropic scale invariance [86]. From the computation of the cumulants of the corresponding self-similarity kernel, we show that there is no way to discriminate between various plausible cascade models recently proposed to account for intermittency in fully developed turbulence and their log-normal approximations. Section 5 is devoted to the experimental demonstration of the existence of an underlying ultrametric hierarchical organization in the WT space-scale representation of the radiance fluctuations. From the unambiguous diagnostic provided by the computation of the "two-point" space-scale correlation functions, we emphasize the log-normal random $\mathcal{W}$-cascade model as a very promising model for simulating the statistical multifractal scaling properties of the Sc internal structure. We conclude in Section 6, by commenting the results of a comparative multifractal analysis of Sc radiance and optical depth fields with those of previous experimental investigations of velocity and temperature fields in high Reynolds number turbulence.

2 Landsat data of marine stratocumulus cloud scenes

Over the past fifteen years, Landsat imagery has provided the remote sensing community at large with a very attractive and reliable tool for studying the Earth's environment [8,12,14–16,21,25,37–41,83,87]. One of the main advantages of high-resolution satellite imagery is its rather low effective cost as compared to outfitting and flying research aircraft. Moreover this instrument is well calibrated and it offers the possibility to reach unusual high spatial, spectral and radiometric resolutions [25,83]. Indeed, the five-channel Multi-Spectral Scanning (MSS, Landsat 1-3) radiometer resolves features down to 80 m with 7 bits of dynamic range. The seven-channel Thematic Mapper (TM, Landsat 4-5) camera does even better with a resolution of 30 m and a dynamic range of 8 bits. Both these instruments are essentially proportional to nadir-viewing radiance at satellite level ($\simeq$ 800 km). Scores of Landsat completely or partially cloudy scenes have thus been acquired, mainly for the purpose of characterizing cloud morphology. Mainly two types of statistical analysis have been applied so far to Landsat imagery: spectral analysis of the 2D radiance field [21,25,37–39,83] and joint area and perimeter distributions for ensembles of individual clouds [12,14–16] defined by some threshold in radiance. One of the most remarkable properties of Landsat cloud scenes is their statistical "scale-invariance" over a rather large range of scales, which justifies why fractal and multifractal concepts have progressively gained more acceptance in the atmospheric scientist community [7,8].

Off all cloud types, marine stratocumulus (Sc) are without any doubt the ones which have attracted the most attention, mainly because of their first-order effect on the Earth's energy balance [6–8,25,83,84]. Being at once very persistent and horizontally extended, marine Sc layers carry considerable weight in the overall reflectance (albedo) of the planet and, from there, command a strong effect on its global climate [9]. Furthermore, with respect to climate modeling [10] and the major problem of cloud-radiation interaction [8,17,20–25,64], they are presumably at their simplest in marine Sc which are relatively thin ($\sim 300-500$ m), with well-defined (quasi-planar) top and bottom, thus approximating the plane-parallel geometry where radiative transfer theory is well developed [6,17,22,23,25,64]. However, because of its internal homogeneity assumption, plane-parallel theory shows systematic biases in large-scale average

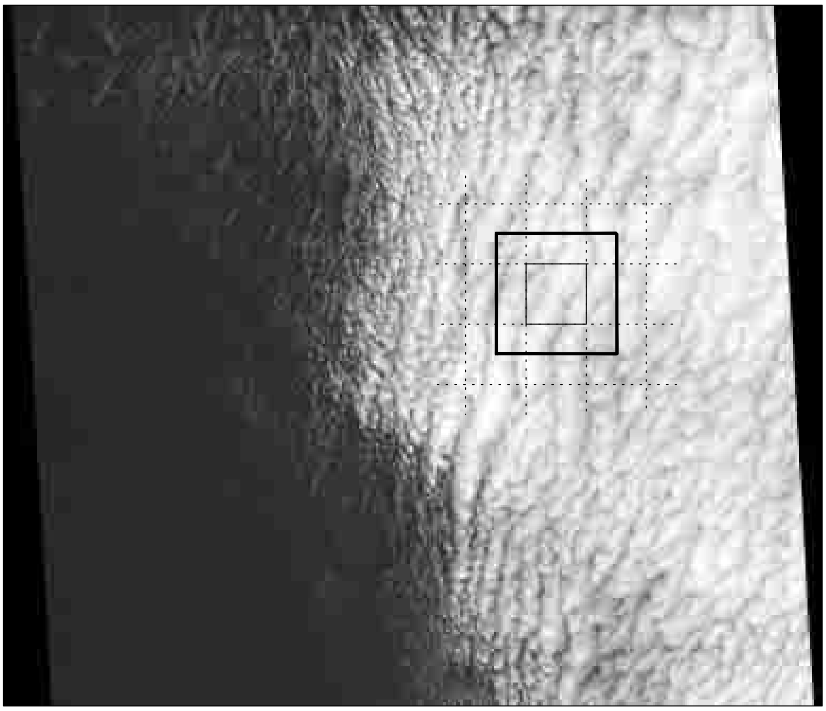

Fig. 1. The original Landsat TM image in the 0.6−0.7 μm channel. This 196×168 km^2 scene was captured at $l = 30$ m resolution on July 7 1987, off the coast of San Diego (Ca) during FIRE [34]. Quasi-nadir viewing radiance at satellite level is digitized on a eight-bit grey scale. The thick black square represents one among the 32 overlapping 1024×1024 pixels^2 portions selected in the cloudy region to carry out our 2D WT multifractal analysis of an extensive marine Sc. The thin black square corresponds to the inner 512×512 central part where our WT computations are safe from (finite size) edge effects. The dashed squares are the neighbouring 512×512 central cloudy portions.

reflectance [23,88] relevant to Global Circulation Model (GCM) energetics and large random errors in small-scale values [64,89] relevant to remote-sensing applications. Indeed, marine Sc have huge internal variability [19,33], not necessarily apparent to the remote observer (see Figs. 1 and 2). The aim of the present study is to challenge previous analysis [8,12,14–16,21,25,37–41,83,87] of Landsat imagery using the 2D WTMM methodology [57,58,86] described in paper I [46], with the specific goal to improving statistical characterization of the highly intermittent radiance fluctuations of marine Sc, a prerequisite for developing better models of cloud structure and, in turn, furthering our understanding of cloud-radiation interaction.

Figure 1 is a grey-scale rendering of the entire ($\simeq 196 \times 168$ km^2) original cloudy Landsat 5 scene captured with the TM camera (1 pixel = 30 m) in the 0.6−0.7 μm channel (*i.e.* reflected solar photons as opposed to their counterparts emitted in the thermal infrared) during the first ISCCP (International Satellite Cloud Climatology Project) Research Experiment (FIRE) field program [34], which took place over the Pacific Ocean off San Diego in summer 1987. Since almost half of the global scene is clear, we will mainly focus our "wavelet transform microscope" [61,62,90–92] on the right half-part of the image in Figure 1, with the specific goal to zooming into the intricate fine structure of marine Sc. In order to master edge effects in the 2D WT computation (see Sect. 4.3 of paper I [46]), we actually select 32 overlapping 1024×1024 pixels^2 subscenes in this cloudy region. The overall extend of the explored area is about 7840 km^2. Figure 2a shows a typical (1024×1024) portion of the original image where the eight-bit grey scale coding of the quasi-nadir viewing radiance clearly reveals the presence of some anisotropic texture induced by convective structures which are generally aligned to the wind direction. When looking at the profiles obtained through 1D cuts in Figures 2c and 2e, one still recognizes the convective rolls as a rather regular structure superimposed to highly irregular and intermittent fluctuations. Figure 3a shows an averaged (over the 32 1024×1024 pixels^2 images) Fourier transform $\ln |\hat{I}(\mathbf{k})|$ of the nadir radiance field which, besides some weak square lattice anisotropy induced by the discretization process, displays some weak anisotropy in the direction $\theta = \arctan(k_y/k_x) = -\pi/6$ ($\pm\pi$). Note that this anisotropy is somehow enhanced at large scales when $k^{-1} = |\mathbf{k}|^{-1}$ becomes larger than the characteristic width ($\lambda \simeq 5-6$ km) of the convective patterns. Thus it is likely to be induced by the characteristic texture generated by convective motions. When plotting $S(k)$ as a function of $k = |\mathbf{k}|$ in logarithmic coordinates in Figure 3b, one can see two distinct scale breaks: one at 0.2−0.4 km and one

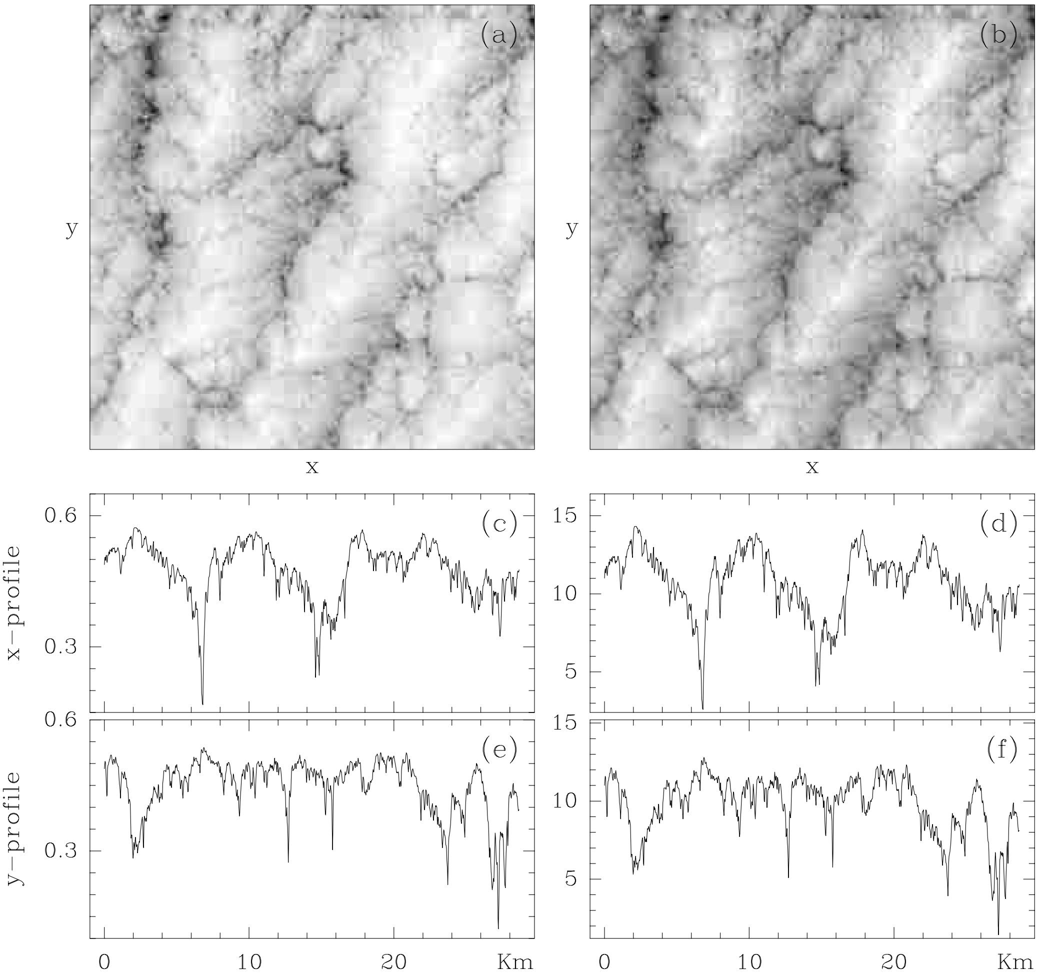

Fig. 2. A 1024 × 1024 pixels^2 portion of the original Landsat TM image shown in Figure 1. Nadir radiance: (a) the cloudy subscene; (c) 1D profile obtained along some horizontal cut; (e) 1D profile obtained along some vertical cut. Optical depth as computed from the nadir radiance using DISORT look-up table for a homogeneous plane-parallel cloud (see Fig. 4): (b) the cloudy sub-scene; (d) some horizontal 1D profile; (f) some vertical 1D profile. $I(\mathbf{x})$ is coded using 256 grey levels from black ($\min I$) to white ($\max I$).

at $\simeq 6$ km. Between these two limits, a rather nice power-law behavior prevails:

$$S(k) \sim k^{-\beta} \qquad (1)$$

with $\beta = 2.72 \pm 0.08$. This value of the spectral exponent is quite compatible with previous estimates obtained for 1D LWC data [21,25–32,37–39,83], namely $\beta_{\rm LWC} = 1.4 - 1.7 \simeq \beta_{\rm 2D} - 1$. The cross-over observed at large scales from $\beta = 2.72$ towards $\beta = 0$ in some way marks the integral scale for marine Sc during FIRE. Indeed this cross-over begins at a scale $\sim 5{-}6$ km which corresponds to the characteristic width of the convective patterns. The statistical significance of this cross-over is that most of the correlations in cloud structure are confined inside the convective rolls and apparently do not propagate from one convective structure to the neighbouring ones. Of course this observation applies for Sc cloudy scenes that usually display convective structures with a width to height ratio of about 2 to 6. The transition at scales $0.2{-}0.4$ km to a spectrum which becomes steeper at smaller scales as the signature of smoother behavior, has been the subject of some controversy in the literature [19,21,25,37–39]. Cahalan and Snider [37] noted that the characteristic scale of the so-called "Landsat scale break" is close to the nominal geometrical thickness for marine Sc. However, *in situ* probings of LWC fluctuations in marine Sc have revealed scale-invariance properties from a few tens of meters to a few tens of kilometers [19,32,33]; no special behavior occurs at cloud thickness scale, nor at that of the whole boundary layer. This makes any dynamical mechanism that may somehow controls internal cloud structure an unlikely explanation for the Landsat scale break. Lovejoy and co-workers [38] have expressed some skepticism as far as the physical relevance of the Landsat scale break. They mainly argued about two technical reasons that might cause a spurious scale break: on the one hand the fact that the Landsat radiometer saturates frequently in cloudy scenes, and on the other hand the fact that many of the published statistical analysis suffer from insufficient sampling. Let us point out that the data used

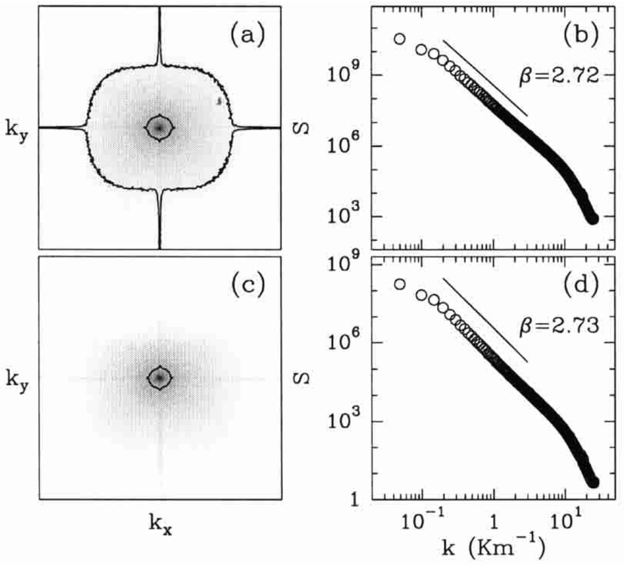

Fig. 3. Power-spectrum analysis of 32 (1024 × 1024) images as the ones shown in Figures 2a and 2b respectively. Nadir radiance: (a) $\ln|\hat{I}(\mathbf{k})|$ as coded using 32 grey levels from white ($\min \ln|\hat{I}|$) to black ($\max \ln|\hat{I}|$); (b) $S(|\mathbf{k}|)$ *vs.* $|\mathbf{k}|$ in logarithmic representation. Optical depth: (c) $\ln|\hat{I}(\mathbf{k})|$; (d) $S(|\mathbf{k}|)$ *vs.* $|\mathbf{k}|$ in logarithmic representation. The fuzzy curves made of small black dots in (a) and (c) are level curves to guide the eyes.

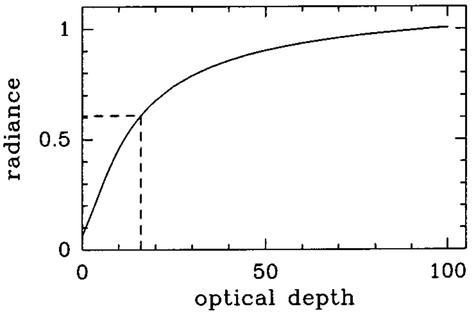

Fig. 4. The plane-parallel optical depth-nadir radiance monotonic nonlinear relation as obtained when using DISORT routines [63]. The rectangle defined by the dashed lines delimits the dynamical range for radiance and optical depth values in the original image (Fig. 1)

in Figures 1 and 2 to obtain the statistics required for the power spectrum analysis reported in Figure 3 is less than 1.25% saturated. Moreover, our set of 32 (1024 × 1024) pixels^2 cloudy scenes is large enough to establish experimentally the statistical convergence of the power spectral exponent β. The best fit to equation (1) between 70 m and 300 m in Figure 3b yields $\beta \simeq 5.0$; but as previously noticed for the analysis of 1D intersects [25], one cannot rule out an exponential cut-off. Our finding are therefore very much in favor of Davis *et al.* [25,65] physical interpretation of the Landsat scale break in terms of net horizontal fluxes excited by the horizontal variability of Sc layers [93–96]. We refer the reader to reference [25], where these authors have succeeded in simulating the Landsat scale break in strictly scaling cloud models, thus confirming that the scale break is actually caused by radiation transport process.

Remark

Note that very much like the so-called bottleneck phenomenon [97–99] observed in the power spectra of fully developed turbulent fields at the wave number corresponding to peak dissipation, the Landsat scale break around 200–400 m involves some energy pile up which diminishes the power-law decay of $S(k)$ prior to the transition to strong damping.

The above discussion raises the crucial issue of up to which extend the fluctuations of the radiance field collected by the Landsat TM camera reflect the internal variability of marine Sc clouds. Previous analysis of LWC fluctuations inside marine Sc during FIRE and ASTEX strongly support the idea that realistic models for cloud optical depth must obey power-law statistics over at least three orders of magnitude in scale [21,25–33,37–39,83]. For FIRE, scaling is actually observed down to 20-40 m, *i.e.*, roughly down to the Landsat pixel-scale. But is there a way to extracting the optical depth field from nadir radiance measurements? In references [23,37,64], Cahalan *et al.* argue that a way to compute radiance escaping from a horizontally inhomogeneous cloud model is to apply the Independent Pixel Approximation (IPA) which amounts to using plane-parallel theory on a pixel basis. In Figure 4 is shown the monotonic nonlinear mapping from the optical depth to the radiance as obtained when using Stammes *et al.*'s DISORT software package [63] to perform plane-parallel radiance computations [25]. Since this mapping is monotonic, one can invert it to transform radiance data into optical depth (pseudo) data. In Figures 2b, 2d and 2f are reported the results of such a transformation; from a simple visual inspection, one does not see any significant change when comparing to the radiance data in Figures 2a, 2c and 2e respectively. From a more quantitative point of view, the results of the power-spectrum analysis of the optical depth in Figures 3c and 3d are remarkably similar to the ones previously obtained for the radiance field. A well-defined power-law behavior with an exponent $\beta = 2.73 \pm 0.08$ is observed over a range of scale that extends from $\sim 300-400$ m up to 5–6 km where a cross-over to a decorrelated "white-noise" behavior is initiated. Below 300–400 m, we still observe a transition to smoother behavior which, according to Davis and co-workers [25,65], should not be there but which is the direct consequence of the inaccuracy of the IPA to model radiation transport in variable media. When using Monte-Carlo simulations that take into account horizontal fluxes (this amounts to relax the IP assumption), these authors [25,65] not only establish the radiative origin of the Landsat scale break, but they also bring evidence for the relevance of the IPA to accurately predicts the fluctuations of the radiance field from the knowledge of the optical depth and *vice versa*, for scales which are larger than some "radiative smoothing"

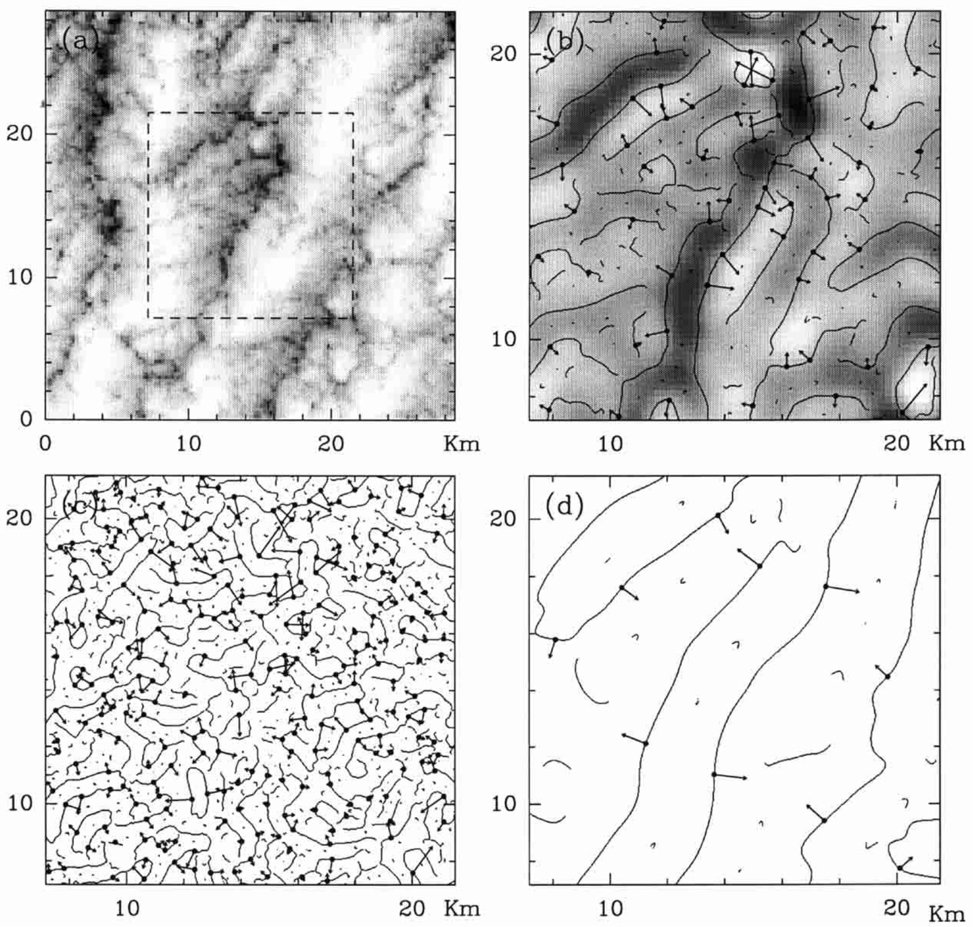

Fig. 5. 2D wavelet transform analysis of a Landsat image of marine Sc clouds. $\boldsymbol{\psi}(\mathbf{x})$ is the first-order radially symmetric analyzing wavelet shown in Figure 1 of paper I [46]. (a) 256 grey-scale coding of a (1024×1024) portion of the original radiance image. In (b) $a = 2^{2.9}\sigma_{\rm W}$, (c) $a = 2^{1.9}\sigma_{\rm W}$ and (d) $a = 2^{3.9}\sigma_{\rm W}$ (where $\sigma_{\rm W} = 13$ pixels $\simeq 390$ m), are shown the maxima chains; the local maxima of $\mathcal{M}_{\boldsymbol{\psi}}$ along these chains are indicated by (●) from which originates an arrow whose length is proportional to $\mathcal{M}_{\boldsymbol{\psi}}$ and its direction (with respect to the x-axis) is given by $\mathcal{A}_{\boldsymbol{\psi}}$; only the central (512×512) part delimited by a dashed square in (a) is taken into account to define the WT skeleton. In (b), the smoothed image $\phi_{\mathbf{b},a} * I$ is shown as a grey-scale coded background from white (min) to black (max).

scale $\eta_{\rm rs} = \sqrt{l_{\rm t}\Delta_z} \sim 200-300$ m, where Δ_z is the cloud's geometrical thickness and $l_{\rm t}$ the transport mean free path.

Remark

Note that the resolution of our 2D WT microscope will not allow us to investigate the Landsat scale break discussed just above. As described in paper I [46], $\sigma_{\rm W} = 13$ pixels (~ 390 m) is the width of the analyzing wavelet at the smallest scale where it is still well enough resolved. Above that scale, we will assume that radiance field data provide almost direct access to the internal structure of marine Sc. This working hypothesis turns out to be quite reasonable since, as seen in Figure 4, the dynamical range of radiance data in the original Landsat image (Fig. 1), does not extend above 0.61 where the nonlinearity of the optical depth-radiance IPA mapping is the most pronounced.

3 Application of the 2D WTMM method to Landsat images of stratocumulus clouds

This section is devoted to the application of the 2D WTMM method [58,86] to the Landsat cloudy scene shown in Figure 1. We systematically follow the numerical implementation procedure described in Section 4.3 of paper I [46]. We first wavelet transform the 32 overlapping (1024×1024) images, cut out of the original image as explained in Section 2, with the first-order ($n_{\boldsymbol{\psi}} = 1$) radially symmetric analyzing wavelet defined in Figure 1 of paper I [46]. To master edge effects, we then restrain our analysis to the (512×512) central part of the wavelet transform of each image. From the wavelet transform skeleton defined by the WTMMM, we compute the partition functions from which we extract the $\tau(q)$ and $D(h)$ multifractal spectra as explained in Section 4.1 of paper I [46]. We systematically test the robustness of our estimates with respect to some change in the shape

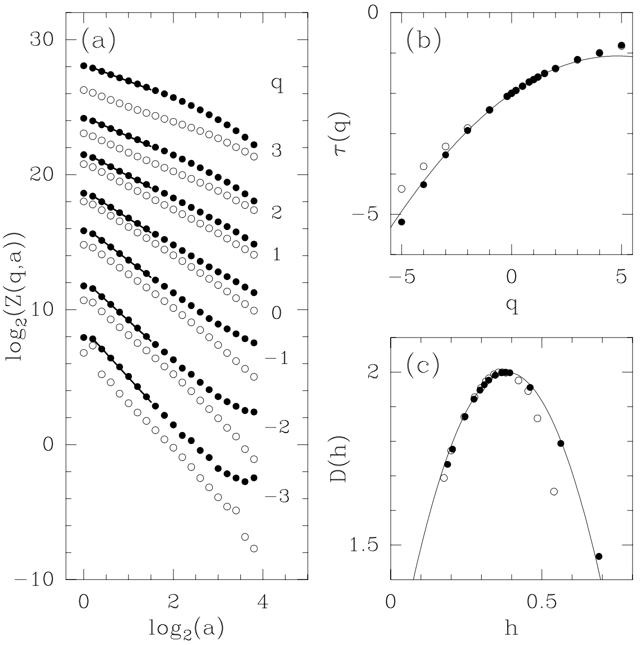

Fig. 6. Determination of the $\tau(q)$ and $D(h)$ spectra of radiance Landsat images of marine Sc. The 2D WTMM method is used with either a first-order (●) or a third-order (○) radially symmetric analyzing wavelet (see Fig. 1 of paper I [46]). (a) $\log_2 \mathcal{Z}(q,a)$ *vs.* $\log_2 a$; the solid lines correspond to linear regression fits of the data over the first and a half octave. (b) $\tau(q)$ *vs.* q as obtained from a linear regression fit of the data in (a). (c) $D(h)$ *vs.* h, after Legendre transforming the $\tau(q)$ curve in (b). In (b) and (c), the solid lines correspond to the theoretical multifractal spectra for log-normal $\mathcal{W}$-cascades with parameter values $m = -0.38 \ln 2$ and $\sigma^2 = 0.07 \ln 2$ (Eqs. (29, 30) in paper II [56]).

of the analyzing wavelet, in particular when increasing the number of zero moments.

3.1 Numerical computation of the multifractal $\tau(q)$ and $D(h)$ spectra

In Figure 5 is illustrated the computation of the maxima chains and the WTMMM for the marine Sc sub-scene shown in Figure 2a. In Figure 5b is shown the convolution of the original radiance field (Fig. 5a) with the isotropic Gaussian smoothing filter ϕ (Eq. (22) of [46]). According to the definition of the WTMM, the maxima chains correspond to well defined edge curves of the smoothed image. The local maxima of $\mathcal{M}_\psi$ along these curves are indicated by (●) from which originates an arrow whose length is proportional to $\mathcal{M}_\psi$ and its direction (with respect to the x-axis) is given by $\mathcal{A}_\psi$. After linking these WTMMM across scales, one constructs the WT skeleton from which one computes the partition functions $\mathcal{Z}(q,a)$ (Eq. (59) of paper I [46]). As reported in Figure 6a, the annealed average partition functions (●) display some well-defined scaling behavior over the first three octaves, *i.e.* over the range of scales $390 \text{ m} \lesssim a \lesssim 3120$ m, when plotted *versus* a in a logarithmic representation. Indeed the scaling deteriorates progressively from the large scale side when one goes to large values of $|q| \gtrsim 3$. In the following, we will see that besides the fact that we are suffering from insufficient sampling, the presence of localized Dirac like structures is likely to explain the fact that the observed cross-over to a steeper power-law decay occurs at a smaller and a smaller scale when one increases $q > 0$. Actually for $q \gtrsim 3$, the cross-over scale $a^* \lesssim 1200$ m becomes significantly smaller than the so-called integral scale which is approximately given by the characteristic width $\lambda \simeq 5$–6 km of the convective rolls (Fig. 5a). When processing to a linear regression fit of the data in Figure 6a over the first octave and a half (in order to avoid any bias induced by the presence of the observed cross-over at large scales), one gets the $\tau(q)$ spectrum (●) shown in Figure 6b. In contrast to the fractional Brownian rough surfaces studied in Section 5 of paper I [46], this $\tau(q)$ spectrum unambiguously deviates from a straight line. When Legendre transforming this nonlinear $\tau(q)$ curve, one gets the $D(h)$ singularity spectrum reported in Figure 6c. Its characteristic single humped shape over a finite range of Hölder exponents is a clear signature of the multifractal nature of the marine Sc radiance fluctuations. As a test of the reliability of our Legendre transform computation, we report in Figure 7 the results (●) of the estimate of the $D(h)$ singularity spectrum from the scaling behavior of the partition functions $h(q,a)$ (Eq. (66) in paper I [46]) and $D(q,a)$ (Eq. (67) of paper I [46]). While $D(q,a)$ in Figure 7b displays a quite well-defined scaling behavior over the entire range of scales represented, namely $390 \text{ m} \lesssim a \lesssim 6240$ m, $h(q,a)$ in Figure 7a exhibits some q-dependent cross-over scale which reminds the cross-over phenomenon observed on $\mathcal{Z}(q,a)$ in Figure 6a. When proceeding to linear regression fits over the first and a half octave in both Figures 7a and 7b, one gets estimates for $h(q)$ and $D(q)$ from which one extracts the $D(h)$ singularity spectrum shown in Figure 7c. The so-obtained $D(h)$ curve (●) is quite indistinguishable from the $D(h)$ spectrum (▲) previously obtained from the Legendre transform of the $\tau(q)$ data. Moreover the "error bars" estimated by varying the range of scales used to perform the linear regression fit for both $h(q,a)$ and $D(q,a)$, give some indication of up to which extend one can trust our data, especially when one increases (decreases) inconsiderately q beyond 3 (-3).

In Figure 6 are also shown for comparison the results (○) obtained when applying the 2D WTMM method with a third-order ($n_\psi = 3$) radially symmetric analyzing wavelet (the smoothing function ϕ being the isotropic 2D mexican hat). As seen in Figure 6a, the use of a wavelet which has more zero moments seems to somehow improve scaling. For the range of q-values investigated in Figure 6a, the cross-over scale turns out to be rejected at a larger scale, enlarging by some amount the range of scales over which scaling properties can be measured, especially for the largest values of $|q|$. This observation is confirmed in Figure 7a where $h(q,a)$ displays a more convincing scaling behavior for $q = 2, 3...$ up to 6. The fact that one improves scaling when increasing the order of the analyzing wavelet suggests that perhaps some

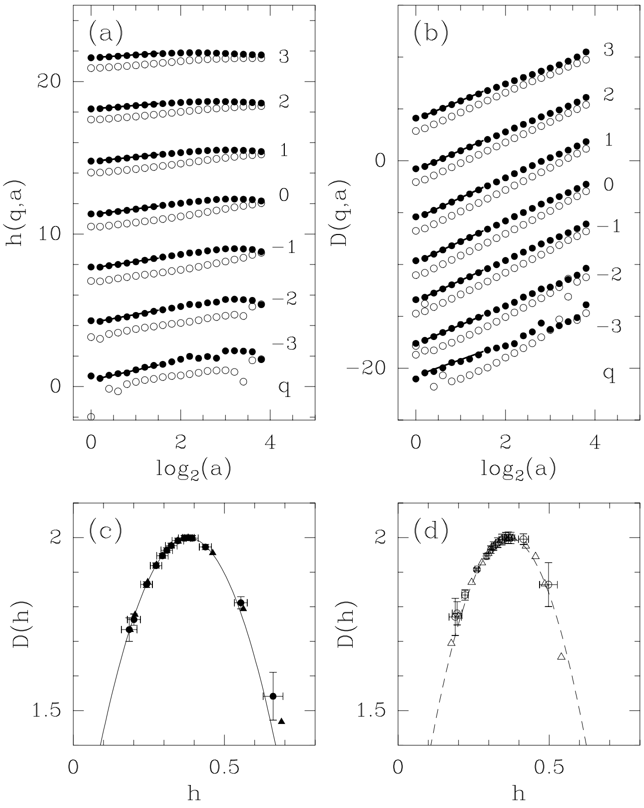

Fig. 7. Determination of the $D(h)$ singularity spectrum of radiance Landsat images of marine Sc. The 2D WTMM method is applied with either a first-order (● and ▲) or a third-order (○ and △) radially symmetric analyzing wavelet. (a) $h(q, a)$ *vs.* $\log_2 a$. (b) $D(q, a)$ *vs.* $\log_2 a$. (c) $D(h)$ *vs.* h, as obtained from a linear regression fit of the data in (a) and (b) over the first and a half octave (●); the symbols (▲) correspond to the $D(h)$ curve after Legendre transforming the $\tau(q)$ data in Figure 6b; $\boldsymbol{\psi}$ is a first-order analyzing wavelet. (d) $D(h)$ *vs.* h, same computation as in (c) but with a third-order analyzing wavelet. In (c) and (d), the solid and dashed lines correspond to parabolic spectra as predicted by the log-normal $\mathcal{W}$-cascade model with parameters: ($m = -0.38 \ln 2$, $\sigma^2 = 0.07 \ln 2$) and ($m = -0.366 \ln 2$, $\sigma^2 = 0.06 \ln 2$) respectively.

smooth behavior unlikely deteriorates our statistical estimate of the multifractal spectra of the original Landsat radiance image. Let us recall that, as explained in Section 3.2 of paper I [46], smooth C^∞ behavior may give rise to maxima lines along which $\mathcal{M}_{\boldsymbol{\psi}} \sim a^{n_{\boldsymbol{\psi}}}$ (see example 1 in Sect. 3.3 of paper I [46]); hence larger $n_{\boldsymbol{\psi}}$ smaller is the overall contribution of those "spurious" maxima lines in the partition function summation over the WT skeleton. As seen in Figures 1 and 2, the anisotropic texture induced by the convective streets or rolls might well be at the origin of the relative lack of well defined scale invariance. When looking at the corresponding $\tau(q)$ spectrum (○) extracted from the data in Figure 6a, using the same linear regression procedure as before, one gets quantitatively the same estimates for $q \gtrsim -1$. For more negative values of q, the data obtained with the third-order analyzing wavelet clearly depart from the previous estimates with the first-order wavelet. The slope of the new $\tau(q)$ spectrum is somehow weakened which implies, from the Legendre transform properties, that the corresponding values of $h(q) = \partial\tau/\partial q$ are reduced. The computation of the $D(h)$ singularity spectrum (○) in Figure 6c enlightens this phenomenon: while the increasing left-hand branch (which corresponds to the strongest singularities) of the $D(h)$ curve appears to be quite robust with respect to the choice of $\boldsymbol{\psi}$, the decreasing right-hand branch (associated to the weakest singularities) is modified when increasing the number of zero moments of $\boldsymbol{\psi}$. This effect is confirmed in Figure 7d, where a remarkably similar narrower (from its right-hand side) $D(h)$ curve is obtained when using $h(q, a)$ and $D(q, a)$ instead of the Legendre transform. As illustrated in Figures 6 and 7, the $D(h)$ spectrum as well as the $\tau(q)$ spectrum data, are very well fitted by the theoretical quadratic spectra predicted for log-normal random $\mathcal{W}$-cascades (Eqs. (29, 30) of paper II [56]), namely

$$\tau(q) = -\frac{\sigma^2}{2\ln 2}q^2 - \frac{m}{\ln 2}q - 2, \tag{2}$$

and

$$D(h) = -\frac{(h + m/\ln 2)^2}{2\sigma^2/\ln 2} + 2. \tag{3}$$

However, with the first-order analyzing wavelet, the best fit is obtained with the parameter values $m = -0.38 \ln 2 = -0.263$ and $\sigma^2 = 0.07 \ln 2 = 0.049$, while for the third-order wavelet these parameters take slightly different values, namely $m = -0.366 \ln 2 = -0.254$ and $\sigma^2 = 0.06 \ln 2 = 0.042$. The variance parameter σ^2 which characterizes the intermittent nature of marine Sc radiance fluctuations is therefore somehow reduced when going from $n_{\boldsymbol{\psi}} = 1$ to $n_{\boldsymbol{\psi}} = 3$. We will see in Section 3.2 that the lack of statistical convergence because of insufficient sampling is actually the main reason for this uncertainty in the estimate of σ^2. As previously experienced in paper II [56] for synthetic multifractal rough surfaces, an accurate estimate of the exponents $\tau(q)$ for $q \lesssim -3$ requires more than 32 (1024×1024) images. With the statistical sample of Landsat images we have at our disposal, one gets $D(h(q = 0) = 0.37 \pm 0.02) = 2.00 \pm 0.01$, which is a strong indication that the radiance field is singular everywhere. From the estimate of $\tau(q = 2) = -1.38 \pm 0.02$; one gets the following estimate of the spectral exponent: $\beta = \tau(2) + 4 = 2.62 \pm 0.02$, *i.e.*, a value which is slightly smaller than the one extracted from the power-law decay of the energy spectrum in Figure 3b. This difference comes from the range of wavevector $|\mathbf{k}|$ used in Figure 3b, which actually corresponds to some shift towards the largest scales as compared to the range of scales selected in Figure 6a for the WTMM computation of the $\tau(q)$ spectrum.

To corroborate the soundness of the last remark raised at the end of Section 2, we have repeated our WTMM computations for the 32 (1024×1024) images of the marine Sc optical depth as reconstructed from the radiance data using DISORT routines [63] (see Fig. 2b). The results are reported in Figure 8, where radiance (●) and

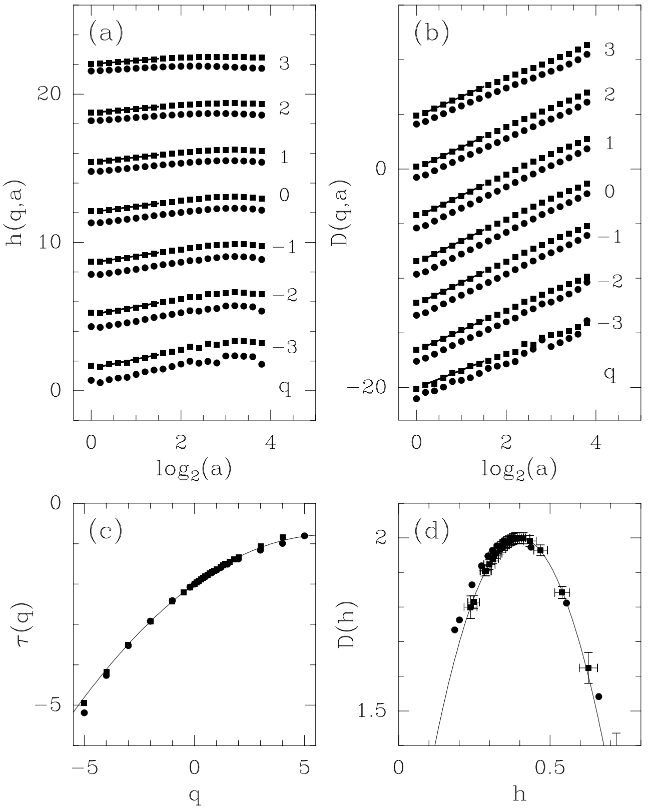

Fig. 8. Determination of the $\tau(q)$ and $D(h)$ multifractal spectra of the radiance (●) and optical depth (■) Landsat data. The analyzing wavelet is the first-order radially symmetric wavelet used in Figure 6. (a) $h(q,a)$ *vs.* $\log_2 a$. (b) $D(q,a)$ *vs.* $\log_2 a$. (c) $\tau(q)$ *vs.* q; same computations as in Figure 6b. (d) $D(h)$ *vs.* h; same computations as in Figure 7c. In (c) and (d), the solid lines correspond to the best quadratic log-normal spectra for the optical depth data with parameter values $m = -0.399 \ln 2$ and $\sigma^2 = 0.065 \ln 2$.

optical depth (■) data are shown for comparison. Clearly, for the range of values of q for which statistical convergence is likely to be achieved ($-3 \lesssim q \lesssim 5$), one does not see any significant difference between the statistical scaling properties of these two fields. The respective $\tau(q)$ and $D(h)$ spectra are indistinguishable as compared to the size of the error bars. This is the confirmation that the radiance fluctuations collected by Landsat TM camera can be considered as a faithful representation of the intermittent internal structure of marine Sc clouds.

3.2 WTMMM probability density functions

This sub-section is mainly devoted to the analysis of the joint probability distribution function $P_a(\mathcal{M}, \mathcal{A})$ (see Sect. 4.2 of paper I [46]) as computed from the wavelet transform skeletons of the 32 (1024 × 1024) radiance images with the first-order radially symmetric analyzing wavelet ($n_{\psi} = 1$) used in Figures 5 [86]. In Figures 9a and 9b are respectively shown the pdf's $P_a(\mathcal{M}) = \int \mathrm{d}\mathcal{A}\, P_a(\mathcal{M}, \mathcal{A})$ and $P_a(\mathcal{A}) = \int \mathrm{d}\mathcal{M}\, P_a(\mathcal{M}, \mathcal{A})$,

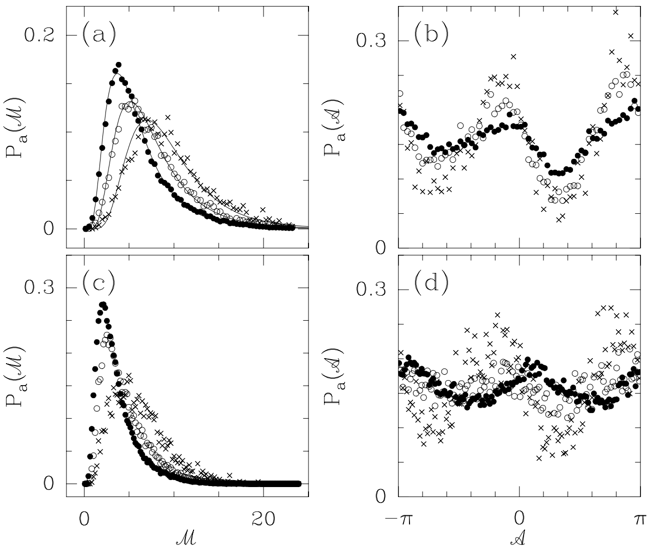

Fig. 9. Pdf's of the WTMMM coefficients of the 32 (1024 × 1024) radiance Landsat images. First-order radially symmetric analyzing wavelet: (a) $P_a(\mathcal{M})$ *vs.* $\mathcal{M}$; (b) $P_a(\mathcal{A})$ *vs.* $\mathcal{A}$; the symbols correspond to the following scales $a = 2^{0.3}\sigma_{\mathrm{W}} = 480$ m (●), $2^{1.3}\sigma_{\mathrm{W}} = 960$ m (○) and $2^{2.3}\sigma_{\mathrm{W}} = 1920$ m (×). Third-order radially symmetric analyzing wavelet: (c) $P_a(\mathcal{M})$ *vs.* $\mathcal{M}$; (d) $P_a(\mathcal{A})$ *vs.* $\mathcal{A}$; the symbols correspond to the scales $a = 2^{0.6}\sigma_{\mathrm{W}} = 591$ m (●), $2^{1.6}\sigma_{\mathrm{W}} = 1182$ m (○) and $2^{2.6}\sigma_{\mathrm{W}} = 2364$ m (×).

for three different values of the scale parameter $a = 2^{0.3}\sigma_{\mathrm{W}}$ (480 m), $2^{1.3}\sigma_{\mathrm{W}}$ (960 m) and $2^{2.3}\sigma_{\mathrm{W}}$ (1920 m). First let us concentrate on the results shown in Figure 9b for $P_a(\mathcal{A})$. This distribution is clearly scale dependent with some evidence of anisotropy enhancement when going from small to large scales, in particular when one reaches scales which become comparable to the characteristic width of the convective structures (*i.e.*, a few kilometers wide). Two peaks around the values $\mathcal{A} \simeq -\pi/6$ and $5\pi/6$ become more and more pronounced as the signature of a privileged direction in the analyzed images. As one can check from a visual inspection of Figures 1 and 2a, this direction is nothing but the perpendicular to the mean direction of the convective rolls that are generally aligned to the wind direction. This is another clear indication that, at large scales, the wavelet transform microscope is sensitive to the convective roll texture, a rather regular modulation superimposed to the background radiance fluctuations [86]. In Figures 9c and 9d are shown for comparison the pdf's $P_a(\mathcal{M})$ and $P_a(\mathcal{A})$ as computed when using a third-order radially symmetric analyzing wavelet ($n_{\psi} = 3$) which is supposed to be less sensitive to smooth behavior. Clearly $P_a(\mathcal{A})$ is much flattened as before and it no longer exhibits some systematic scale dependence. This observation is an important step towards the demonstration that the background radiance fluctuations actually display nearly isotropic scale invariance.

Another important message which comes out from our analysis is illustrated in Figure 10. When conditioning the pdf of $\mathcal{M}$ by the argument $\mathcal{A}$, the shape of this pdf is

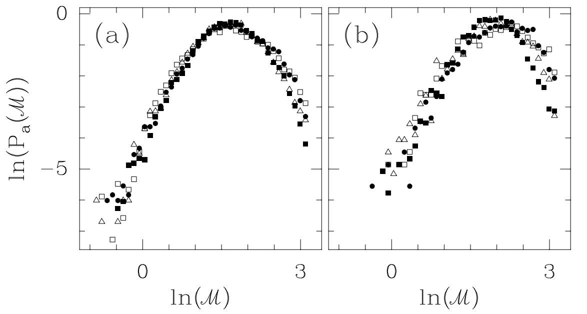

Fig. 10. Pdf's of the WTMMM coefficients of the 32 (1024 × 1024) radiance Landsat images as computed with a first-order radially symmetric analyzing wavelet. Pdf's of $\mathcal{M}$ when conditioned by $\mathcal{A}$. The different symbols correspond to fixing $\mathcal{A}$ (mod π) to $0 \pm \pi/8$ (○), $\pi/4 \pm \pi/8$ (□), $\pi/2 \pm \pi/8$ (△) and $3\pi/4 \pm \pi/8$ (■). (a) $a = 2^{0.3}\sigma_{\rm W} = 480$ m; (b) $a = 2^{1.3}\sigma_{\rm W} = 960$ m.

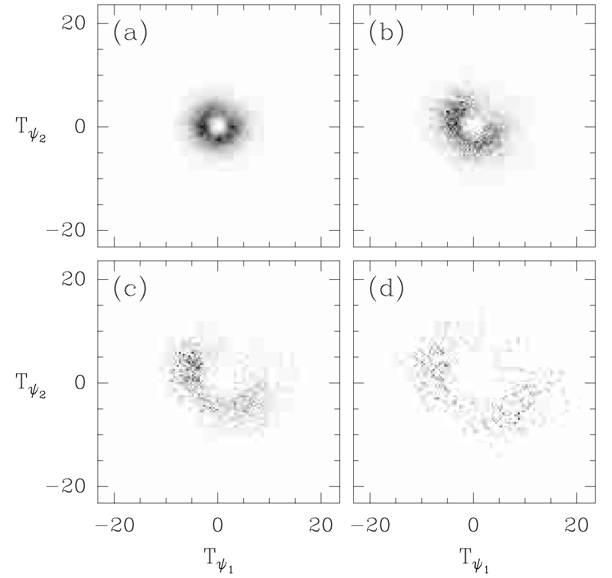

Fig. 11. Distribution of the WTMMM in the plane (T_{ψ_1}, T_{ψ_2}) for the following values of the scale parameter: (a) $a = \sigma_{\rm W} = 390$ m; (b) $a = 2\sigma_{\rm W} = 780$ m; (c) $a = 2^2\sigma_{\rm W} = 1560$ m and (d) $a = 2^3\sigma_{\rm W} = 3120$ m. $\boldsymbol{\psi}$ is a first-order radially symmetric analyzing wavelet. Same 2D WTMM computations as in Figures 9a and 9b.

shown to be independent of the considered value of $\mathcal{A}$, as long as the value of the scale parameter a remains small as compared to the characteristic width of the convective structures. The observation that the joint probability distribution actually factorizes, *i.e.*,

$$P_a(\mathcal{M}, \mathcal{A}) = P_a(\mathcal{M}) P_a(\mathcal{A}), \tag{4}$$

is the signature that $\mathcal{M}$ and $\mathcal{A}$ are likely to be independent [86]. This actual decoupling of $\mathcal{M}$ and $\mathcal{A}$ does not clearly materialize in Figure 11 where the WTMMM are plotted in the (T_{ψ_1}, T_{ψ_2}) plane (see Sect. 2 of paper I [46]) for four values of the scale parameter a. What shows up from the evolution of the distribution of the WTMMM is that, despite the rarefaction of the maxima lines in the WT skeleton when increasing a, more we approach the size of the characteristic width of the convective structures, more this distribution is angularly concentrated around $\mathcal{A} = -\pi/6$ and $5\pi/6$.

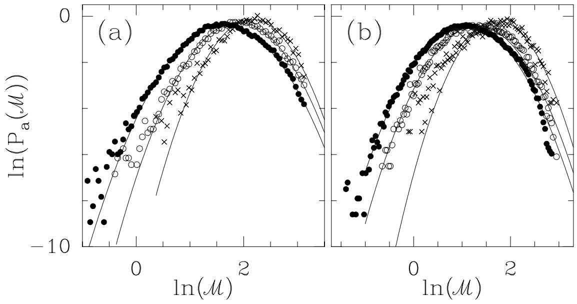

Fig. 12. Pdf's of the WTMMM coefficients of the 32 (1024 × 1024) Landsat radiance images: $\ln(P_a(\mathcal{M}))$ *vs.* $\ln(\mathcal{M})$. (a) First-order radially symmetric analyzing wavelet ($n_{\boldsymbol{\psi}} = 1$); (b) third-order radially symmetric analyzing wavelet ($n_{\boldsymbol{\psi}} = 3$). The symbols have the same meaning as in Figures 9a and 9c respectively. The solid lines are parabola to guide the eyes.

The validity of equation (4) implies that all the multifractal properties of the marine Sc radiance fluctuations are contained in the way the shape of the pdf of $\mathcal{M}$ evolves when one decreases the scale parameter a [86]. This evolution is illustrated in Figure 9a when using a first-order radially symmetric analyzing wavelet. Since by definition the WTMMM are different from zero, $P_a(\mathcal{M})$ decreases exponentially fast to zero at zero. As previously emphasized in paper I [46], this observation is at the heart of the 2D WTMM method which, for this reason, does not suffer any divergency problem when estimating the $\tau(q)$ spectrum for $q < 0$. When plotting $\ln P_a(\mathcal{M})$ *vs.* $\ln \mathcal{M}$, one gets in Figure 12a the remarkable result that for any scale significantly smaller than the integral scale ($\sim$ 5−6 km, as given by the characteristic width of the convective structures), all the data points fall, within a good approximation, on a parabola. This is a strong indication that the WTMMM have a log-normal statistics. As shown in Figure 12b, this experimental feature is not specific to some particular shape of the analyzing wavelet since log-normal pdf's are also found when using a third-order radially symmetric analyzing wavelet. As explained in Section 5.3 of paper I [46], a way to check whether statistical convergence is likely to be achieved is to represent $\mathcal{M}^q P_a(\mathcal{M})$ *versus* $\mathcal{M}$. Indeed, according to equation (70) of paper I [46], the integral of $\mathcal{M}^q P_a(\mathcal{M})$ is proportional to the partition function $\mathcal{Z}(q, a)$ whose scaling exponents $\tau(q)$ are key quantities in the multifractal WTMM description. Even more clever is to look for the following rescaling properties [57,58]:

$$a^{-qh} \mathcal{M}^q P_a(\mathcal{M}) = \mathbb{F}_q(\mathcal{M}/a^h), \tag{5}$$

where $\mathbb{F}_q$ are q-dependent functions that do not depend upon the scale parameter a. As experienced in Section 5.3 of paper I [46] for fractional Brownian surfaces, monofractal scaling implies that there exists a unique exponent

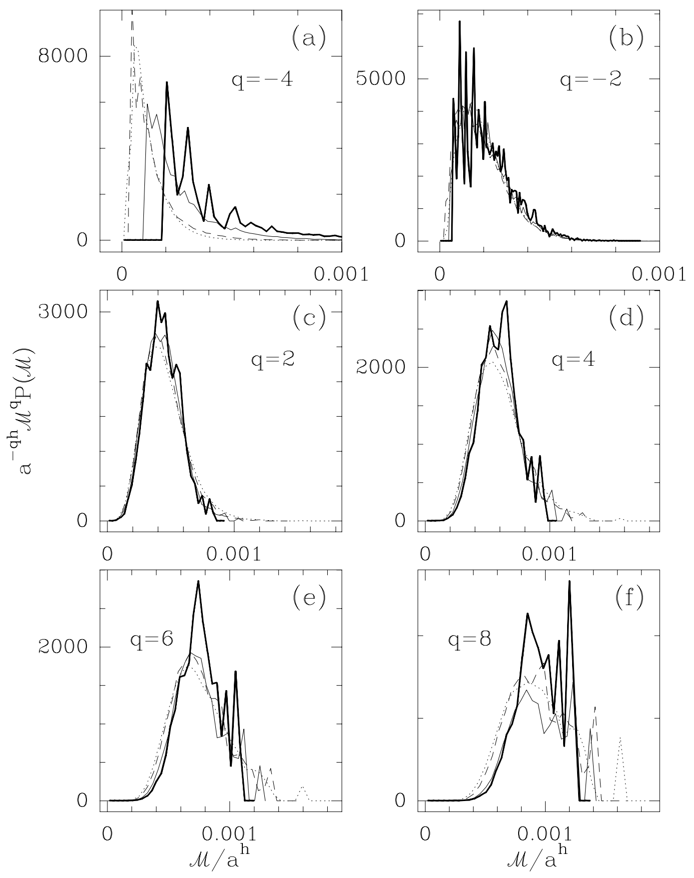

Fig. 13. Pdf's of the WTMMM coefficients of 32 (1024×1024) multifractal rough surfaces generated with the log-normal random $\mathcal{W}$-cascade model (Sect. 2.2 in paper II [56]) for the parameter values $m = -0.38 \ln 2$ and $\sigma^2 = 0.03 \ln 2$. $a^{-qh(q)} \mathcal{M}^q P_a(\mathcal{M})$ *vs.* $\mathcal{M}/a^{h(q)}$ for $q = -4$ (a), -2 (b) 2 (c), 4 (d), 6 (e) and 8 (f). The different curves correspond to the following scales: $a = \sigma_{\rm W}$ (...), $2\sigma_{\rm W}$ (_ _ _), $2^2\sigma_{\rm W}$ (___) and $2^3\sigma_{\rm W}$ (___). $\boldsymbol{\psi}$ is the first-order radially symmetric analyzing wavelet shown in Figure 1 of paper I [46].

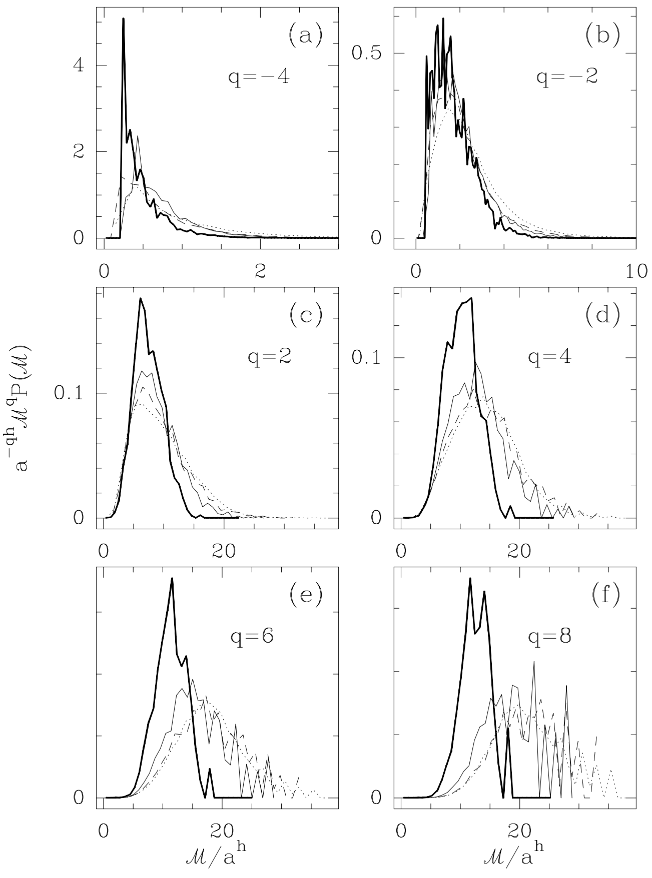

Fig. 14. Pdf's of the WTMMM coefficients of the 32 (1024×1024) radiance Landsat images as computed with a first-order radially symmetric analyzing wavelet ($n_{\boldsymbol{\psi}} = 1$). $a^{-qh(q)} \mathcal{M}^q P_a(\mathcal{M})$ *vs.* $\mathcal{M}/a^{h(q)}$ for $q = -4$ (a), -2 (b) 2 (c), 4 (d), 6 (e) and 8 (f). The different curves correspond to the following scales: $a = \sigma_{\rm W} = 390$ m (...), $a = 2\sigma_{\rm W} = 780$ m (_ _ _), $a = 2^2\sigma_{\rm W} = 1560$ m (___) and $a = 2^3\sigma_{\rm W} = 3120$ m (___).

$h = H$, independent of q, such that equation (5) is verified. As illustrated in Figure 13, equation (5) is still valid for multifractal rough surfaces generated with the log-normal random $\mathcal{W}$-cascade model introduced in Section 2.2 of paper II [56], provided the exponent h be systematically adjusted to the value $h = h(q) = \partial\tau/\partial q$. For $q \in [-3, 8]$, all the data collected at different scales actually collapse on a rather well defined single humped shape distribution which clearly depends upon q, in good agreement with equation (5). Because of the progressive lack of statistics when one increases a, the distributions obtained at the largest scales become more and more noisy. This means that the integral of these distributions, *i.e.*, $\mathcal{Z}(q, a)/\mathcal{Z}(q = 0, a)$, is less and less accurately estimated at large scales. As illustrated in Figure 13a, for $q = -4$, there is no longer a well defined $\mathbb{F}_q$ distribution whatever the value of the scale a; this means that we are faced with insufficient sampling when computing $\mathcal{Z}(q, a)$ and in turn $\tau(q)$, for $q \lesssim -3$. One can already perceived in Figure 13f, that a similar lack of statistical convergence is already attained for $q \gtrsim 8$.

In Figure 14 are shown the results of a similar analysis of the $\mathcal{M}$-pdf's of the radiance Landsat images as computed with a first-order radially symmetric analyzing wavelet (see Fig. 9a). As compared to the numerical results for the synthetic rough surfaces in Figure 13, it is clear that when plugging into equation (5), the values of $h(q)$ obtained from a linear regression fit of the data of $h(q, a)$ *vs.* $\log_2 a$ over the first and a half octave in Figure 7a, one does not get a very spectacular collapse, except at small scales. This is another way to evidence the cross-over observed at large scales in Figures 7a and 8a. Furthermore, more we increase $q > 0$, more pronounced is the separation of the single humped shape distributions obtained at different scales. Let us point out that the fact that those distributions are shifted to the left (*i.e.*, to smaller values of $\mathcal{M}/a^h(q)$), when a is increased, means that $h(q)$ is somehow overestimated. This is not such a surprise since

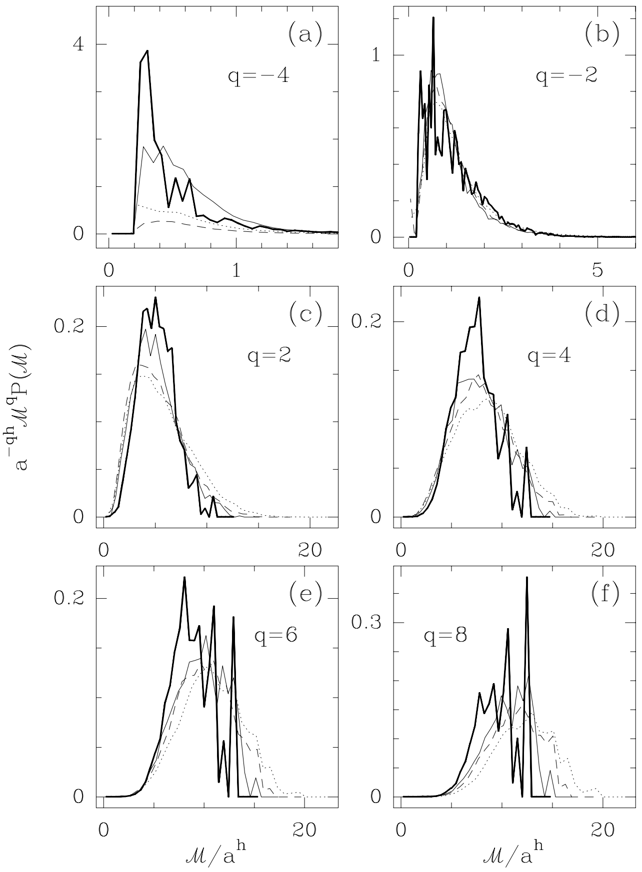

Fig. 15. Pdf's of the WTMMM coefficients of the radiance Landsat images as computed with a third-order radially symmetric analyzing wavelet ($n_\psi = 3$). Same representation as in Figure 14.

as seen in Figure 7a, for $q = 3$, $h(q, a)$ *versus* $\log_2 a$ increases at small scales ($h(q) > 0$) up to some cross-over scale where it starts decreasing ($h(q) < 0$). We will see in the next sub-section that this cross-over behavior is the signature of the presence of very strong singularities with negative Hölder exponents in the radiance images. As far as statistical convergence is concerned, one realizes that for $q \lesssim -3$ as well as for $q \gtrsim 6$, the distributions become very noisy. These poorly resolved distributions explain *a posteriori* the impossibility to get reliable estimate of the $\tau(q)$ exponents for $q \lesssim -3$ and $q \gtrsim 6$ in Figure 6. In Figure 15 are reported the results of the same WTMMM analysis of the radiance Landsat images except that now the analyzing wavelet ψ is a third-order radially symmetric wavelet. For each value of $q \gtrsim -2$, the collapse of the distributions obtained at different scales is definitely improved, in particular for the scales much smaller than the integral scale. The shift to the left of the distributions observed in Figure 14 when increasing a, has almost disappeared. It is clear that one does not feel as strong as before the presence of localized structures associated with negative Hölder exponents. On the contrary, for $q \lesssim -3$, the distributions look more different than in Figure 14. This is some indication that the estimates of $\tau(q)$ for $q \leq -3$ are more sensitive to finite sampling with the third-order analyzing wavelet than with the first-order analyzing wavelet. This may explain the underestimation of the intermittency parameter σ^2 in Figure 7d. The results reported in Figures 14 and 15 therefore strongly suggest that, up to finite sampling effects, the relation (5) is valid for the background radiance fluctuations in marine Sc clouds. We will see in the next sub-section that an even more convincing check of the relevance of equation (5) can be obtained if one removes from the WT skeleton, the maxima lines that are associated to rather localized structures corresponding to very strong singularities with negative Hölder exponents [60–62,91,92,100–102].

3.3 Uncovering localized structures in Landsat radiance images

As experienced in previous analysis of fully developed turbulent fields [60–62,91,92,100–102], statistical scale invariance can be disturbed by the presence of isolated localized structures that behave as very strong "quasi" singularities associated to negative Hölder exponent values. Originally discovered in a pioneering wavelet analysis of Modane wind tunnel velocity data [100], the understanding of these rare and intense events in terms of vorticity filaments has been recently confirmed in some swirling turbulent flow experiments [103–105] especially designed for simultaneous visual observation and pressure recording. Vorticity filaments actually appear as very deep pressure drops that can be distinguished from the background pressure fluctuations from their Dirac pulse like behavior [104–109]. In reference [101], we have shown that the continuous wavelet transform is a very powerful tool to detect those multi-scale structures (we refer the reader to the work of Abry and co-workers [107–109] who have proposed an alternative strategy based on the discrete orthogonal wavelet decomposition). When focusing the WT microscope on a strong depression, this pulse-like structure appears as a very strong singularity (*i.e.*, a Dirac peak) when one continuously increases magnification from the integral scale down to the scale of the filament core below which the pressure signal is smooth. The maxima lines corresponding to these very strong "quasi" singularities can be easily distinguished from the other maxima lines in the WT skeleton since, when sliding along these lines from large scales down to small scales, the WTMMM coefficients anomalously increase ($h < 0$) instead of decreasing as commonly observed for singularities with Hölder exponent $h > 0$ [60–62,91,92,100–102]. Our goal in this sub-section is to use the same strategy for the analysis of radiance Landsat images in order to check whether similar "anomalous" maxima lines actually do exist in the corresponding WT skeletons.

In Figure 16a, is shown a 256×256 pixel^2 portion of the original radiance Landsat image of marine Sc clouds (Fig. 1). On this image, the symbols ($\circ$) identify the locations of the roots of some maxima lines computed with a first-order radially symmetric wavelet, along which the WT modulus behaves "anomalously" as shown in

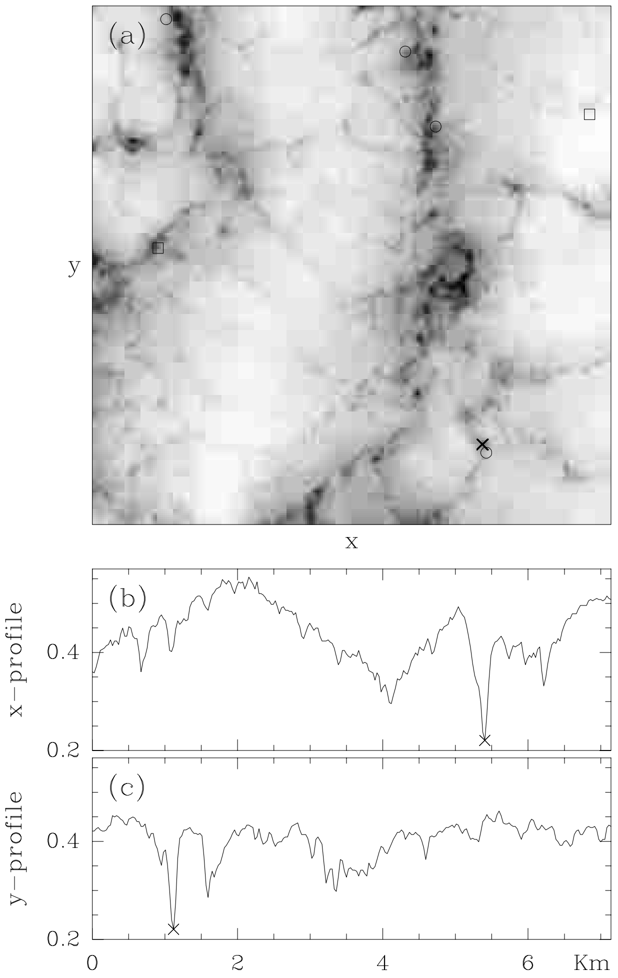

Fig. 16. A 256×256 pixel^2 portion of the original Landsat TM image shown in Figure 1. The symbols correspond to locations where point to some "anomalous" maxima lines along which the WTMMM increase when going from large to small scales as reported in Figure 17b. $\boldsymbol{\psi}$ is a first-order (○) or a third-order (□) radially symmetric analyzing wavelet. In (b) and (c) are respectively represented the horizontal and vertical 1D radiance profiles obtained when crossing the localized downward spike event identified by the symbol (×) in (a).

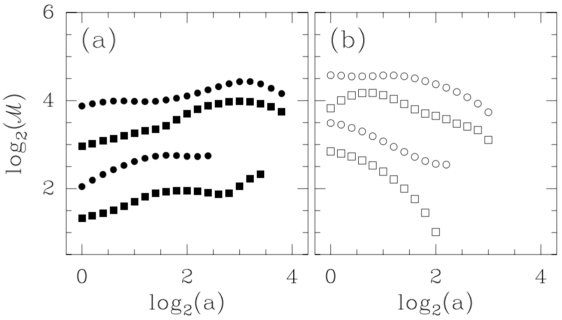

Fig. 17. Characterizing the local Hölder regularity of the radiance fluctuations from the behavior of the WTMMM along the maxima lines: $\log_2(\mathcal{M}_{\boldsymbol{\psi}})$ *vs.* $\log_2 a$. (a) Maxima lines associated with background radiance fluctuations ($h > 0$). (b) Maxima lines associated with localized downward spike events ($h < 0$). $\boldsymbol{\psi}$ is a first-order (●, ○) or a third-order (■, □) radially symmetric analyzing wavelet.

Figure 17. In Figure 17a is represented the behavior of $\log_2(\mathcal{M}_{\boldsymbol{\psi}})$ *vs.* $\log_2 a$ as obtained along most of the maxima lines (●) that belong to the WT skeleton. Despite the presence of some oscillations, one observes a rather convincing power-law decrease from large scales to small scales with a slope which takes values in the range $0.1 \lesssim h(\mathbf{x}_0) \lesssim 0.7$, *i.e.*, in some interval which is included in the support of the $D(h)$ singularity spectrum previously computed in Figures 6c and 7c. In Figure 17b is reported the behavior observed on some maxima lines (○), along which some rather convincing power-law increase from large scales to small scales, witnesses to the presence of unusually strong singularities with Hölder exponent $h \lesssim -0.5$. When looking at 1D intersects of the radiance field that cross those particular points, one gets profiles similar to the ones illustrated in Figures 16b and 16c. These special points correspond to strong localized events that remind the intermittently distributed downward spikes observed in LWC measurements during FIRE and ASTEX programs [32, 33]. Some tentative interpretation of these downspikes as probable dry air entrained from cloud top and carried by penetrating downdrafts has been proposed by Davis *et al.* [32]. As seen in Figure 16a, when using a third-order radially symmetric analyzing wavelet which is less sensitive to the smooth envelop contribution of the convective patterns, one discovers that these localized downward spikes (□) are not systematically located along the edges of the convective rolls but can also be found as isolated localized structures. There is no doubt that these rather rare anomalously strong singularities should not disturb too much the scaling behavior of the partition functions $\mathcal{Z}(q,a)$ and $h(q,a)$ in Figures 6a and 7a for small values of $|q|$. Because they correspond to isolated singularities, the corresponding number of maxima lines in the WT skeleton is constant across scales as compared to the high rate of proliferation $N(a) \sim a^{-2}$ of the maxima lines associated to the most frequently observed Hölder exponent, namely $h(q = 0) = 0.37 \pm 0.02$. But as soon as one increases $q \gtrsim 3$, the statistical contribution of these anomalous maxima lines becomes less and less negligible as compared to the set of maxima lines associated with the leading singularities of Hölder exponents $h \simeq h(q)$. Therefore, one can expect to observe the signature of the presence of these very strong singularities mainly at large scales where their statistical contribution is likely to become very quickly competitive when increasing q. This is actually what is observed in Figures 6a and 7a where for $q = 3$, one already notices some cross-over at a scale $a^* = 2\sigma_{\mathrm{W}}$ ($\simeq 780$ m), for both $\mathcal{Z}(q,a)$ and $h(q,a)$. (Note that this cross-over scale may depend upon the shape of the analyzing wavelet.) The fact that this cross-over scale clearly decreases when increasing q is quite consistent with the above scenario. A way to improve scaling would thus consist in discriminating in the WT skeleton, the maxima lines induced by those localized downward spike like structures from those corresponding to background radiance fluctuations. As previously experienced

in reference [101] when identifying vorticity filaments from background pressure fluctuations in swirling turbulent flows, such a discrimination requires some rather rigorous operational protocol. The results reported in Figure 17b are only specific examples of the presence of strongly localized downward spike events in radiance Landsat images. We hope to report on a more systematic study of those intermittent events in a forthcoming publication.

4 WTMM computation of the self-similarity kernel of radiance Landsat images

We have seen in Section 3.2, that the joint probability distribution $P_a(\mathcal{M},\mathcal{A})$ of the WTMMM coefficients of the radiance Landsat images is likely to satisfy the factorization relationship (4) that ensures the statistical independence of the modulus and the argument of the WTMMM. As exemplified on multifractal rough surfaces generated with the random $\mathcal{W}$-cascade model in Section 4 of paper II [56], under this factorization condition, one can use the 2D wavelet based deconvolution method [86] described in Section 4.1 of paper II [56], to compute the so-called self-similarity kernel $G_{aa'}$ which accounts for the evolution of the shape of $P_a(\mathcal{M})$ when going from a coarse scale a' to a smaller scale a:

$$P_a(\mathcal{M}) = \int G_{aa'}(u) P_{a'}(\mathrm{e}^{-u}\mathcal{M})\mathrm{e}^{-u}\mathrm{d}u, \text{ for } a' > a. \quad (6)$$

As demonstrated in paper II [56], if one notes

$$M(p,a) = \int \mathrm{e}^{\mathrm{i}p\ln\mathcal{M}} P_a(\mathcal{M})\mathrm{d}\mathcal{M}, \quad (7)$$

the characteristic function associated with the WTMMM logarithms at scale a, then the Fourier transform $\hat{G}$ of the kernel G can be computed from the ratio:

$$\hat{G}_{aa'}(p) = \frac{M(p,a)}{M(p,a')}, \quad (8)$$

provided $M(p,a')$ do not vanish. According to the definition of continuously self-similar cascades [78,110–113], $\hat{G}_{aa'}$ should be of the form:

$$\hat{G}_{aa'}(p) = \hat{G}(p)^{s(a,a')}, \quad (9)$$

where $s(a,a')$ accounts for the number of elementary cascade steps from scale a' to scale a ($s(a)$ can be seen as the number of steps from the "integral" scale L down to the considered scale a). According to Novikov's definition [75], the cascade is scale-similar (or scale-invariant) if:

$$s(a,a') = \ln(a'/a), \quad (10)$$

i.e., $s(a) = \ln(L/a)$.

In order to test the validity of equation (9), let us first focus on the scale dependence of $\hat{G}_{aa'}$, as computed with equation (8). Figures 18a and 18c respectively show the modulus logarithm ($\ln|\hat{G}_{aa'}|$) and the phase ($\Phi_{aa'}$) of $\hat{G}_{aa'}$, for various pairs of scales $a < a'$, as computed from the WT skeleton of the 32 (1024 × 1024) radiance Landsat images using a first-order radially symmetric wavelet ($n_\psi = 1$) [86]. In Figures 18b and 18d respectively, we succeed in collapsing all different data in Figures 18a and 18c onto a single kernel $\hat{G}(p) = \hat{G}_{aa'}^{1/s(a,a')}(p)$, with $s(a,a') = \ln(a'/a)$ in good agreement with equations (9) and (10) and the continuously scale-invariant self-similar cascade picture. Let us point out that this collapse starts deteriorating for $|p| \gtrsim 4$, mainly as the consequence of finite size effects as well as of some insufficient sampling as previously experienced in Section 4 of paper II [56] when analyzing synthetic rough surfaces generated by the random $\mathcal{W}$-cascade model. But there is some additional reason here for the observed departure from general collapse for $|p| \gtrsim 4$, which is the presence of the localized downward spike structures discovered in Section 3.3. These "dirac" like isolated events are identified by the wavelet transform microscope as very strong singularities ($h < 0$) which definitely perturb the statistical scaling properties of the background radiance fluctuations when one increases $p \gtrsim 4$. Nevertheless, as illustrated by a solid line in Figures 18b and 18d, a log-normal kernel, *i.e.*, a parabola for $\ln|\hat{G}(p)|$ and a straight line for $\Phi(p)$, provide remarkable fits of the data in the range $-4 \lesssim p \lesssim 4$. As

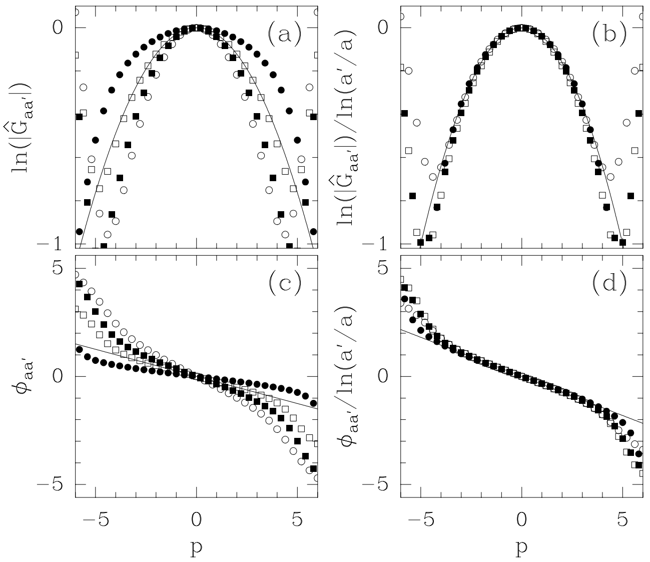

Fig. 18. Estimation of $\hat{G}_{aa'}(p)$ for 32 (1024 × 1024) radiance Landsat images. The analyzing wavelet is the first-order radially symmetric wavelet shown in Figure 1 of paper I [46]. (a) $\ln|\hat{G}_{aa'}(p)|$ *vs.* p; (b) $\ln|\hat{G}_{aa'}(p)|/\ln(a'/a)$ *vs.* p; (c) $\Phi_{aa'}(p)$ *vs.* p; (d) $\Phi_{aa'}(p)/\ln(a'/a)$ *vs.* p. The symbols correspond to the following pairs of scales: $a = 2^{0.5}\sigma_\mathrm{W} = 551$ m, $a' = 2^{2.5}\sigma_\mathrm{W} = 2204$ m (○); $a = 2^{1.5}\sigma_\mathrm{W} = 1102$ m, $a' = 2^{2}\sigma_\mathrm{W} = 1560$ m (●); $a = 2\sigma_\mathrm{W} = 780$ m, $a' = 2^{2}\sigma_\mathrm{W} = 1560$ m (□); $a = 2\sigma_\mathrm{W} = 780$ m, $a' = 2^{2.5}\sigma_\mathrm{W} = 2204$ m (■). In (b) and (d), the solid lines correspond to the theoretical log-normal kernel $\hat{G}(p) = \exp[(imp - \sigma^2p^2/2)/\ln 2]$, for the parameter values $m = -0.38\ln 2$ and $\sigma^2 = 0.08\ln 2$.

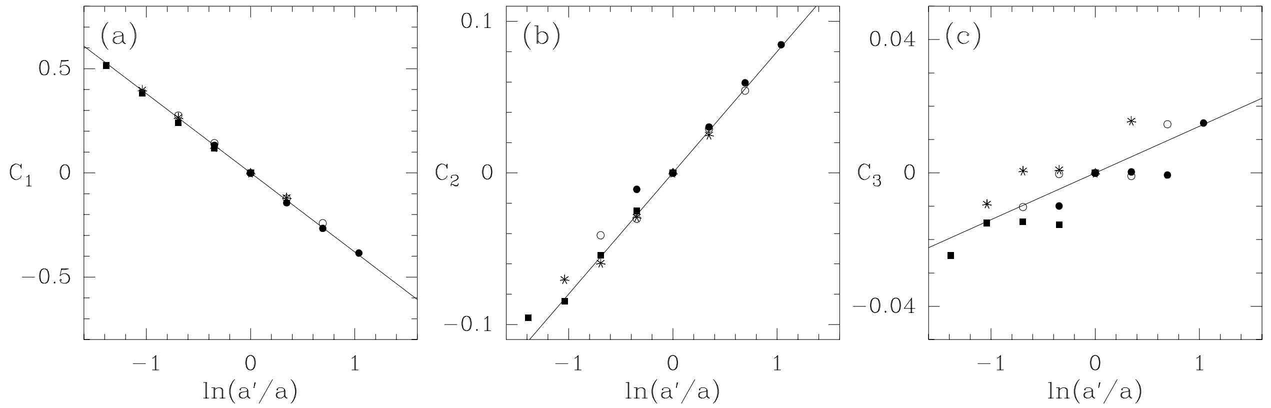

Fig. 19. Computation of the cumulants of the self-similarity kernel $\hat{G}$ of the radiance Landsat images. ψ is the first-order radially symmetric analyzing wavelet. (a) $C_1(a,a')$ *vs.* $\ln(a'/a)$; (b) $C_2(a,a')$ *vs.* $\ln(a'/a)$; (c) $C_3(a,a')$ *vs.* $\ln(a'/a)$. The symbols correspond to the following values of the reference scale $a' = 2^{0.5}\sigma_{\mathrm{W}} = 551$ m ($\bullet$), $2\sigma_{\mathrm{W}} = 780$ m ($\circ$), $2^{1.5}\sigma_{\mathrm{W}} = 1102$ m ($*$) and $2^2\sigma_{\mathrm{W}} = 1560$ m ($\blacksquare$). The solid lines correspond to linear regression fit estimates of the cumulants: $c_1 = -0.38 \pm 0.01$, $c_2 = 0.08 \pm 0.01$ and $c_3 = 0.014 \pm 0.005$.

discussed in Section 4.2 of paper II [56], one can proceed to a quantitative estimate of the cumulants c_k of G:

$$\hat{G}(p) = \exp\left(\sum_{k=1}^{\infty} c_k \frac{(\mathrm{i}p)^k}{k!}\right), \tag{11}$$

via the computation of

$$\begin{aligned} C_{2n+1}(a,a') &= (-1)^n \partial^{2n+1}\Phi_{aa'}/\partial p^{2n+1}|_{p=0}, \\ &= c_{2n+1} s(a,a'), \end{aligned} \tag{12}$$

and

$$\begin{aligned} C_{2n+2}(a,a') &= \partial^{2n+2} \ln|\hat{G}_{aa'}|/\partial p^{2n+2}|_{p=0}, \\ &= c_{2n+2} s(a,a'), \end{aligned} \tag{13}$$

for $n \geq 0$. In Figure 19 are reported the results of a linear regression fit of $C_1(a,a')$, $C_2(a,a')$ and $C_3(a,a')$ when plotted *versus* $\ln(a'/a)$, for different values of the reference scale a'. For both C_1 and C_2, one gets for the first two cumulants, values which corroborate the parametrization of the $\tau(q)$ data in Figure 6b, namely $c_1 = m/\ln 2 = -0.38 \pm 0.01$ and $c_2 = \sigma^2/2 = 0.08 \pm 0.01$. Let us recall at that point the expression that links $\tau(q)$ to the cumulants c_k (Eq. (64) in paper II [56]):

$$\tau(q) = -\sum_{k=1}^{\infty} c_k \frac{q^k}{k!} - 2. \tag{14}$$

Note that the fact that all the data points fall on a same straight line in both Figures 19a and 19b corroborates the existence of scale invariant properties as long as the scale parameter $a \lesssim 2^{2.5}\sigma_{\mathrm{W}}$ (2204 m) remains small enough as compared to the integral scale. It is clear on Figure 19c that scale invariance is no longer obvious on the behavior of $C_3(a,a')$ *vs.* $\ln(a'/a)$. As previously discussed in section 4 of paper II [56], the computation of c_3 and higher-order cumulants requires incredibly high sampling in order to control statistical convergence. If we try to compare the experimental data in Figure 19c to the numerical data in Figures 26c and 28c in paper II [56] for respectively log-normal and log-Poisson synthetic rough surfaces, one may be tempted to conclude that our estimate of $c_3 = 0.014 \pm 0.005$ bring evidence for some departure from the log-normal $\mathcal{W}$-cascade scenario ($c_k = 0$, $\forall k \geq 3$). (Let us point out that on the contrary to c_1 and c_2, the estimate of c_3 is quite unstable and depends strongly on the investigated range of scales.) In order to avoid a too hurried conclusion, let us use the convolution equation (6) to collapse all the WTMMM pdf's computed at different scales in Figure 9a onto a single curve, using either the full self-similarity kernel G with $c_1 = -0.38$, $c_2 = 0.08$ and $c_3 = 0.014$ as obtained in Figure 19, or its log-normal approximation by fixing $c_3 = 0$. As shown in Figure 20,

a remarkably good collapse is obtained either way which is not surprising since the fact that c_3 may be different from zero is governed by the tail of $P_a(\mathcal{M})$ at large $\mathcal{M}$ values which, as seen in Figure 20a, is rather noisy because of insufficient sampling. This means that one must not be abused by the strikingly good collapse of the tails of $P_a(\mathcal{M})$ in Figure 20c, which looks more spectacular, because of the smoothing effect of the self-similarity kernel in the convolution equation (6), than expected as regards to the highly fluctuating tails observed in Figure 20a for 551 m $\leq a \leq$ 2204 m. The WTMM computation of the self-similarity kernel of the radiance Landsat images of marine Sc clouds therefore confirms the existence of an underlying scale-invariant self-similar cascade structure; but with the available set of experimental data, there is no way to discriminate between various phenomenological cascade models recently proposed to account for intermittency and their log-normal approximations.

Remark

Let us note that the estimate of the intermittency parameter from the computation of the second cumulant of G, namely $c_2 = \sigma^2/\ln 2 = 0.08$, is slightly larger than

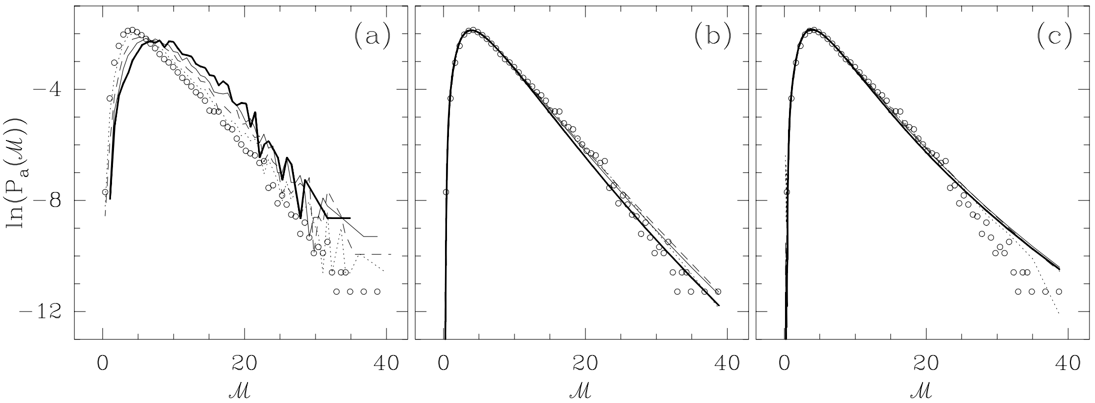

Fig. 20. Pdf's of $\mathcal{M}$ as computed at different scales $a = 2^{0.5}\sigma_W = 551$ m (○), $2\sigma_W = 780$ m (…), $2^{1.5}\sigma_W = 1102$ m (_ _ _), $2^2\sigma_W = 1560$ m (___) and $2^{2.5}\sigma_W = 2204$ m (___). $\boldsymbol{\psi}$ is the first-order radially symmetric analyzing wavelet. Same computations as in Figure 9a. (a) $\ln P_a(\mathcal{M})$ *vs.* $\mathcal{M}$. (b) $\ln P_a(\mathcal{M})$ *vs.* $\mathcal{M}$; same data as in (a) but after being transformed according to equation (6) with a Gaussian kernel build from the first two cumulants estimated in Figures 19a and 19b, namely $c_1 = -0.38$ and $c_2 = 0.08$. (c) Same pdf's as in (a) but after being transformed with a kernel build from the first three cumulants estimated in Figure 19, namely $c_1 = -0.38$, $c_2 = 0.08$ and $c_3 = 0.014$.

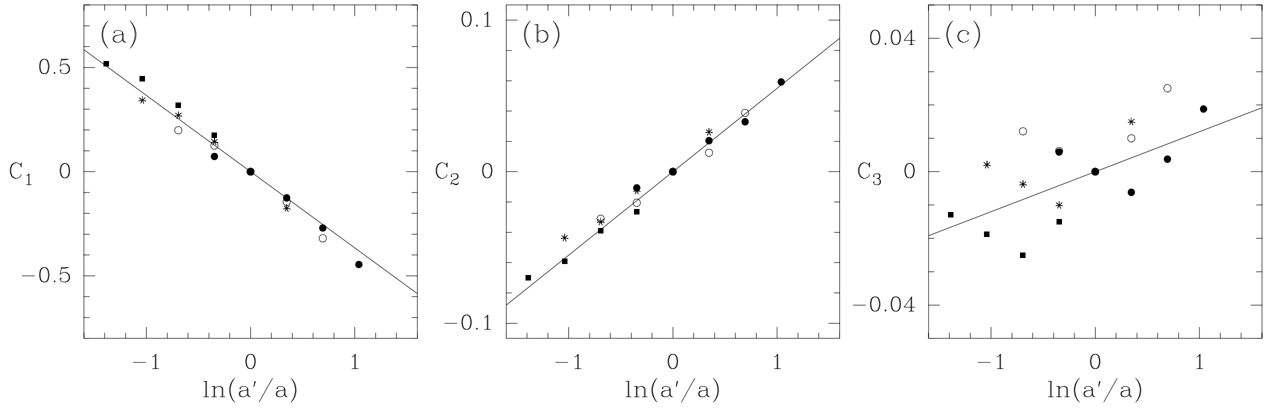

Fig. 21. Computation of the cumulants of the self-similarity kernel $\hat{G}$ of the radiance Landsat images. $\boldsymbol{\psi}$ is the third-order radially symmetric analyzing wavelet. (a) $C_1(a, a')$ *vs.* $\ln(a'/a)$; (b) $C_2(a, a')$ *vs.* $\ln(a'/a)$; (c) $C_3(a, a')$ *vs.* $\ln(a'/a)$. The symbols correspond to the following values of the reference scale $a' = \sigma_W = 390$ m (●), $2^{0.5}\sigma_W = 551$ m (○), $2\sigma_W = 780$ m ($*$), $2^{1.5}\sigma_W = 1102$ m (■) and $2^2\sigma_W = 1560$ m (□). The solid lines correspond to linear regression fit estimates of the cumulants: $c_1 = -0.37 \pm 0.01$, $c_2 = 0.055 \pm 0.01$ and $c_3 = 0.012 \pm 0.005$.

the value obtained from the best parabolic fit of the $\tau(q)$ data in Figure 6b, namely $\sigma^2/\ln 2 = 0.07$. This difference is actually significative of the degree of accuracy of our numerical estimate: $\sigma^2/\ln 2 = 0.075 \pm 0.010$.

The above conclusion is indeed corroborated by the results of similar studies carried out with higher-order analyzing wavelets. In Figure 21 are plotted $C_1(a, a')$, $C_2(a, a')$ and $C_3(a, a')$ *versus* $\ln(a'/a)$, as computed with a third-order radially symmetric analyzing wavelet. The data still indicate the existence of scale invariance; all the points corresponding to values of a and a' in the range $[\sigma_W, 2^{2.5}\sigma_W]$ ([390 m,2204 m]), fall again on a same straight line. From linear regression fit of the data in Figures 21a and 21b, one gets the following estimates for the first two cumulants: $c_1 = -0.37 \pm 0.01$ and $c_2 = 0.055 \pm 0.010$, which are in good agreement with the values obtained in Figure 7d from the parametrization of the $D(h)$ data. We thus confirm the slight difference previously observed in the WTMM estimates (Figs. 7c and 7d) of the intermittency exponent $c_2 = \sigma^2/\ln 2$ when using analyzing wavelets of different orders. As already pointed out when comparing the distributions obtained in Figures 14 and 15 with respectively a first-order and a third-order analyzing wavelet, this difference shows that the requirement of statistical convergence is more and more demanding when further increasing the order of the analyzing wavelet. As far as the estimate of the third cumulant in Figure 21c, the spreading of the data points about some hypothetic increasing straight line makes us very cautious as regard to this very poor evidence of statistical convergence. The result of the linear regression fit $c_3 = 0.012 \pm 0.005$ is just given for comparison with the previous estimate in Figure 19c.

Remark

Let us mention that we have performed similar computations of the self-similarity kernel for the 32 (1024×1024)

images of the marine Sc optical depth as reconstructed from the radiance data using DISORT routines [63] (see Fig. 2b). The results so obtained are quite indistinguishable from those reported in Figures 18, 19, 20 and 21 for the radiance field. This is not such a surprise after the remarkable agreement found in Figure 8 for the respective $\tau(q)$ and $D(h)$ spectra.

5 Space-scale correlation function analysis of radiance Landsat images

As pointed out in previous works [113–116], the real demonstration of the existence of an underlying multiplicative structure consists in taking advantage of the space-scale unfolding provided by the continuous wavelet transform, to compute the cross-scale correlation functions. This "two-point" statistical analysis amounts to compute the correlations of the logarithms of the amplitude of a space-scale decomposition of the signal. The so-called magnitude of the function f at the point $\mathbf{x}$ and scale a can be defined using the wavelet transform skeleton:

$$\omega(\mathbf{x}, a) = \ln\Big(\mathcal{M}_{\boldsymbol{\psi}}[f]\big(\mathcal{L}_{\mathbf{x}}(a)\big)\Big), \tag{15}$$

where $\mathcal{L}_{\mathbf{x}}(a)$ is a maxima line that points to the points $\mathbf{x}$ in the limit $a \to 0$. As originally defined in reference [114] for 1D signals and generalized in 2D in Section 5.1 of paper II [56], one can use an alternative definition which is based on the continuous wavelet transform and which does not require the computation of the WTMMM:

$$\omega(\mathbf{x}, a) = \frac{1}{2} \ln \varepsilon^2(\mathbf{x}, a), \tag{16}$$

where

$$\varepsilon^2(\mathbf{x}, a) = a^{-4} \int \chi((\mathbf{x} - \mathbf{y})/a) |T_{\boldsymbol{\psi}}[f](\mathbf{y}, a)|^2 \mathrm{d}^2\mathbf{y}. \tag{17}$$

This means that instead of working with the WTMMM, one works with some average of $|T_{\boldsymbol{\psi}}|^2$ over some interval centered at $\mathbf{x}$ and of size a ($\chi(\mathbf{x})$ is a bump function such that $||\chi||_1 = 1$). As defined in equation (68) of paper II [56], the space-scale magnitude correlations consist in computing:

$$C(\mathbf{x_1}, \mathbf{x_2}; a_1, a_2) = \langle \tilde{\omega}(\mathbf{x_1}, a_1) \tilde{\omega}(\mathbf{x_2}, a_2) \rangle, \tag{18}$$

where $\langle \dots \rangle$ stands for ensemble average and $\tilde{\omega}$ for the centered process $\omega - \langle \omega \rangle$.

As documented in references [113,114] and Section 5 of paper II [56], a scale invariant multiplicative process can be revealed by a characteristic scale independent slow decay of its space-scale magnitude correlation functions:

$$C(\Delta x = |\boldsymbol{\Delta}\mathbf{x}|, a_1, a_2) \sim \sigma^2 \log_2 \left(\frac{L}{\Delta x} \right), \qquad \text{when} \quad \sup(a_1, a_2) \le \Delta x < L, \tag{19}$$

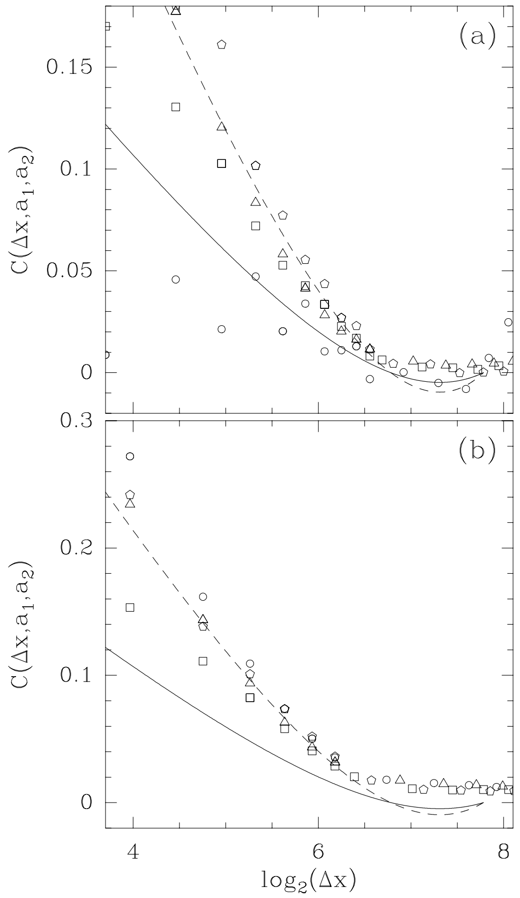

Fig. 22. Magnitude correlation function $C(\Delta x, a_1, a_2)$ *vs.* $\log_2(\Delta x)$, as computed from the 32 (1024×1024) radiance Landsat images using a first-order radially symmetric analyzing wavelet. (a) WTMMM magnitude: $\omega(\mathbf{x}, a) = \ln[\mathcal{M}_{\boldsymbol{\psi}}[f](\mathcal{L}_{\mathbf{x}}(a))]$ (Eq. (15)). (b) Continuous WT magnitude: $\omega(\mathbf{x}, a) = \frac{1}{2} \ln \varepsilon^2(\mathbf{x}, a)$ (Eq. (16)). The symbols have the following meaning: $a_1 = a_2 = 2\sigma_{\mathrm{W}} = 780$ m (○); $a_1 = \sigma_{\mathrm{W}} = 390$ m, $a_2 = 2\sigma_{\mathrm{W}} = 780$ m (△); $a_1 = \sigma_{\mathrm{W}} = 390$ m, $a_2 = 4\sigma_{\mathrm{W}} = 1560$ m (□); $a_1 = 2\sigma_{\mathrm{W}} = 780$ m, $a_2 = \sigma_{\mathrm{W}} = 1560$ m (◇). The solid (dashed) lines correspond to the theoretical prediction (Eq. (20)) for multifractal rough surfaces generated with the random $\mathcal{W}$-cascade model with parameters $\sigma^2 = 0.08 \ln 2$ ($0.16 \ln 2$) and $L = 220$ pixels $= 6.6$ km.

after some averaging over all the pairs of points separated by a spatial distance Δx. In Figure 22 are reported the results of the computation of $C(\Delta x, a_1, a_2)$ when averaging over the 32 (1024×1024) radiance Landsat images, using either the WTMMM (Fig. 22a) or the continuous WT (Fig. 22b) definition of the magnitude of f (Eqs. (15, 16) respectively). One can see that, for $\Delta x > \sup(a_1, a_2)$, all the data points fall, in good approximation, onto a unique curve when plotted *versus* $\log_2(\Delta x)$, independently of the considered pair of scales (a_1, a_2). Moreover, a straight line of slope $-\sigma^2 = -0.012$ provides a rather reasonable fit of the data up to a separation distance $\Delta x \simeq 2^7$ pixels $\simeq 3.8$ km, where decorrelation seems to be attained. Note that the fact of using the WTMMM instead of the continuous WT does not make any difference; this is a strong indication of the existence of some ultrametric properties underlying the branching structure of the space-scale wavelet representation of the radiance fluctuations. On the top of the data in both Figures 22a and 22b, we have shown, for comparison, the theoretical prediction for the "two-scale" correlation function of multifractal rough surfaces generated by the random $\mathcal{W}$-cascade model (Eq. (76) in paper II [56]):

$$C(\Delta x, a_1, a_2) = \sigma^2 \left(\log_2\left(\frac{L}{\Delta x}\right) - 2 + 2\frac{\Delta x}{L}\right), \quad \text{when } \sup(a_1, a_2) \leq \Delta x < L. \qquad (20)$$

This formula provides a reasonable fit of the data when adjusting the model parameters to $\sigma^2 = 0.16 \ln 2$ and $L = 220$ pixels $= 6.6$ km. While the estimate of the integral scale seems to be of the right order of magnitude as regard to the characteristic width ($\lambda \sim 5$–6 km) of the convective rolls, the value obtained for the intermittency parameter σ^2 is about twice bigger than previous estimates derived from the WTMM computation of the $\tau(q)$ and $D(h)$ multifractal spectra in Figures 6 and 7 and of the self-similarity kernel in Figure 19. At this point, let us emphasize that a similar discrepancy has been previously noticed in the WTMM analysis of wind tunnel turbulent velocity fields [114,116]. It may suggest that simple scale-invariant self-similar cascades as pictured by the random $\mathcal{W}$-cascade model are not sophisticated enough to account for the space-scale structure of the radiance fluctuations in marine Sc clouds. The interpretation of this feature in terms of correlations between weights at a given cascade step or in terms of a more complex geometry of the tree underlying the multiplicative structure of the radiance field is under progress. The possible importance of the intermittently distributed localized downward spike structures is also under consideration. Before drawing definite conclusions, there is clearly a need to repeat the "two-point" correlation function analysis on the background radiance fluctuations, once all the maxima lines corresponding to those Dirac like singularities be removed from the WT skeleton. As a test of the robustness of the above results, we show in Figure 23 the results of a similar analysis when using a higher-order analyzing wavelet. Whatever the shape of the analyzing wavelet, one still gets very strong evidence for some scale-invariant ultrametric structure underlying the intermittent nature of the marine Sc radiance data. Let us point out that similar convincing results are obtained when analyzing the optical depth reconstructed data.

6 Discussion

To summarize, we have reported the results of the experimental application of the 2D WTMM method, introduced in paper I [46] and numerically tested on synthetic multifractal rough surfaces in paper II [56], to radiance Landsat images of marine Sc clouds collected during FIRE program. The computation of the $\tau(q)$ and $D(h)$ spectra have definitely quantified the multifractal scaling properties of both the radiance and the optical depth (computed using DISORT routines [63]) fields. Besides the presence of rather isolated localized downward spike events, the internal cloud structure is clearly intermittent and displays rather convincing isotropic scaling over a range of scale that extend from our WT microscope resolution ($\sigma_W = 13$ pixels $= 390$ m) up to $L/2$, where $L \sim 5$–6 km is some integral scale which is apparently dictated by the average characteristic width of the convective rolls that modulate the amplitude of radiance fluctuations. The additional computation of the self-similarity kernel and of the "space-scale" correlation functions further confirms the existence of some ultrametric space-scale organization that can be understood in terms of a continuous scale-invariant self-similar log-normal multiplicative process [86].

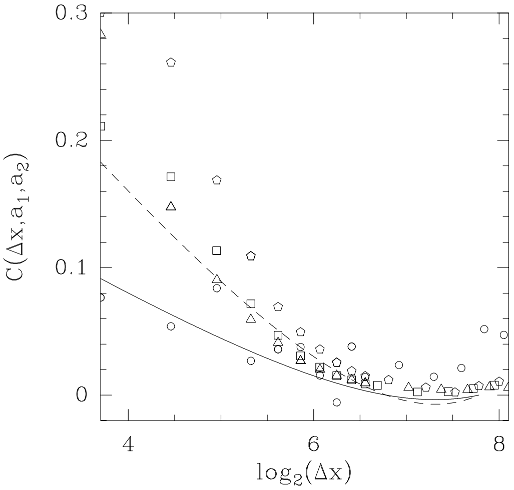

Fig. 23. Magnitude correlation function $C(\Delta x, a_1, a_2)$ *vs.* $\log_2(\Delta x)$, as computed from the 32 (1024×1024) radiance Landsat images using a third-order radially symmetric analyzing wavelet. WTMMM magnitude: $\omega(\mathbf{x}, a) = \ln[\mathcal{M}_{\psi}[f](\mathcal{L}_{\mathbf{x}}(a))]$ (Eq. (15)). The symbols have the same meaning as in Figure 22. The solid (dashed) lines correspond to the theoretical prediction (Eq. (20)) for multifractal rough surfaces generated with the random $\mathcal{W}$-cascade model with parameters $\sigma^2 = 0.06 \ln 2$ ($0.12 \ln 2$) and $L = 220$ pixels $= 6.6$ km.

Let us point out that a similar 1D WTMM analysis of the velocity fluctuations in high Reynolds number turbulence has come to conclusions very close to those of the present study [111,112,114,116,117]. Besides the presence of rather localized Dirac like structures that witness to the probing of vorticity filaments [91,92,100–102], the multifractal nature of turbulent velocity is likely to be understood in terms of a log-normal cascading process which is expected to be scale-invariant in the limit of very high Reynolds numbers [116,117]. In Figure 24 are shown for comparison the results obtained in Figure 7 for the $D(h)$ singularity spectrum of the radiance Landsat images together with the $D(h)$ data extracted from the 1D analysis of a turbulent velocity signal recorded at the Modane wind tunnel ($R_\lambda \simeq 2000$) [112,116] (indeed $D(h) + 1$ is represented for the latter in order to

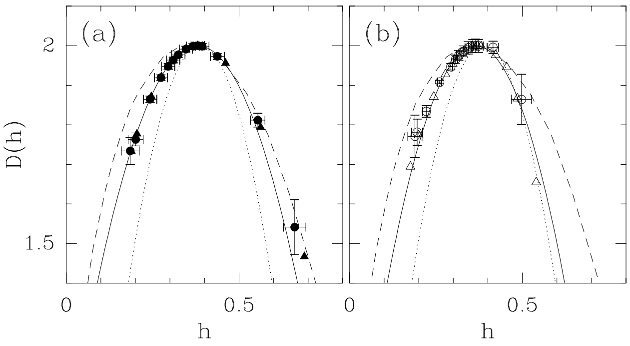

Fig. 24. $D(h)$ singularity spectrum of the radiance Landsat images as computed with the 2D WTMM method using a first-order (a) or a third-order (b) radially symmetric analyzing wavelet. Same computations as in Figures 7c and 7d respectively. The solid lines correspond to the log-normal quadratic spectrum with $m = -0.38 \ln 2$, $\sigma^2 = 0.08 \ln 2$ (a) and $m = -0.366 \ln 2$, $\sigma^2 = 0.06 \ln 2$ (b). The $D(h)$ singularity spectrum of velocity (dotted lines) and temperature (dashed lines) fluctuations in fully developed turbulence are shown for comparison.

compare 1D to 2D data). The turbulent velocity $D(h)$ spectrum significantly differs from the results obtained for the marine Sc cloud. They have a common feature, *i.e.*, the Hölder exponent the most frequently encountered in the radiance field $h = m/\ln 2 = h(q = 0) = \partial\tau/\partial q|_{q=0} = 0.38 \pm 0.01$ is indistinguishable from the corresponding exponent $h = h(q = 0) = 0.39 \pm 0.01$ found for the turbulent velocity field. Note that these values are significantly larger than the theoretical value $h = 1/3$ predicted by Kolmogorov in 1941 [118] to account for the observed $k^{-5/3}$ power-spectrum behavior. The main difference comes from the intermittency parameter which is much stronger for the cloud, $\sigma^2/\ln 2 = 0.08 \pm 0.01$ ($n_\psi = 1$) or $\sigma^2/\ln 2 = 0.06 \pm 0.01$ ($n_\psi = 3$) than for the turbulent velocity, $\sigma^2/\ln 2 = 0.036 \pm 0.004$. This is the signature that the radiance field is much more intermittent than the velocity field: the $D(h)$ singularity spectrum for the former is unambiguously wider than the corresponding spectrum for the later. (Let us recall that insufficient sampling is probably at the origin of the underestimation of the intermittency parameter $c_2 = \sigma^2/\ln 2$ when using a third-order analyzing wavelet. This means that one must not pay too much attention to the decreasing right-hand part of the $D(h)$ cloud data in Fig. 24b.) For the sake of comparison, we have also reported in Figure 24, the multifractal $D(h)$ spectrum of the temperature fluctuations recorded in a $R_\lambda = 400$ turbulent flow [119]. The corresponding single humped curve is definitely much wider than the velocity $D(h)$ spectrum and it is rather close to the data corresponding to the marine Sc radiance field. It is well recognized however that liquid water is not really passive and that its identification with a passive component in atmospheric dynamics offers limited insight into cloud structure since, by definition, near-saturation conditions prevail and latent heat production affects buoyancy [41]. So cloud microphysical processes are expected to interact with the circulation at some, if not all, scales [120]. Nevertheless, our results in Figure 24 tell us that from a multifractal point of view, the intermittency captured by the Landsat satellite looks statistically equivalent to the intermittency of a passive scalar in fully-developed 3D turbulence. The fact that the internal structure of Sc cloud somehow reflects some statistical properties of atmospheric turbulence is not such a surprise in this highly turbulent environment. The investigation of different sets of Landsat data is urgently required in order to test the degree of generality of the results reported in this first WTMM analysis of high-resolution satellite images. In particular, one may wonder up to which extend the marine Sc Landsat data collected off the coast of San Diego on July 7, 1987 under specific observation conditions, actually reflect the specific internal structure of Sc clouds. Work in this direction is currently in progress and we hope to be able to answer this rather fundamental question in a forthcoming publication.

Finally, with respect to the issue of cloud modeling, it comes out quite naturally from the WTMM analysis of marine Sc Landsat data, that the 2D random $\mathcal{W}$-cascade models introduced in Section 2.2 of paper II [56], are much more realistic hierarchical models than commonly used multifractal models like the fractionally integrated singular cascade [49–51,54,83] or the bounded cascade models [84,85]. We are quite optimistic in view of using the log-normal $\mathcal{W}$-cascade models with realistic parameter values for radiation transfer simulations. To our opinion, random $\mathcal{W}$-cascade models are a real breakthrough, not only for the general purpose of image synthesis, but more specifically for cloud modeling. It is likely that better cloud modeling will make further progress in our understanding of cloud-radiation interaction possible.

We are very grateful to R.F. Cahalan, A. Davis, A. Marshak, L. Oreopoulos and J.F. Muzy for helpful discussions. We are very indebted to Y. Gagne, Y. Malecot and S. Ciliberto for the permission to use their experimental turbulent signals. This work was supported by NATO (Grant n° CRG 960176) and was performed while S.G. Roux held a National Research Council–NASA/GSFC Research Associateship.

References

1. A.S. Monin, A.M. Yaglom, *Statistical Fluid Mechanics* (MIT Press, Cambridge, MA, 1975), Vol. 2.
2. U. Frisch, S. Orzag, Physics Today 24 (1990).
3. U. Frisch, *Turbulence* (Cambridge Univ. Press, Cambridge, 1995).
4. *Turbulence: A Tentative Dictionary*, edited by P. Tabeling, O. Cardoso (Plenum, New York, 1995).
5. S. Lovejoy, Science **216**, 185 (1982).
6. R.F. Cahalan, in *Advances in Remote Sensing and Retrieval Methods*, edited by A. Deepak, H. Fleming, J. Theon (Deepak Pub, Hampton, 1989), p. 371.
7. *Fractals in Geoscience and Remote Sensing, Image Understanding Research Series, vol. 1, ECSC-EC-EAEC*, edited by G. G. Wilkinson, J. Kanellopoulos, J. Megier (Brussels, Luxemburg, 1995).

8. A. Davis, A. Marshak, R.F. Cahalan, W.J. Wiscombe, preprint (1997).
9. V. Ramanatahn, R.D. Cess, E.F. Harrison, P. Minnis, B.R. Barkston, E. Ahmad, D. Hartmann, Science **243**, 57 (1989).
10. R.D. Cess *et al.*, Science **245**, 513 (1989).
11. F.S. Rys, A. Waldvogel, in *Fractal in Physics*, edited by L. Pietronero, E. Tosatti (North-Holland, Amsterdam, 1986), p. 461.
12. R.M. Welch, B.A. Wielicki, Clim. Appl. Meteorol. **25**, 261 (1986).
13. J.I. Yano, Y. Takeuchi, J. Meteor. Soc. Japan **65**, 661 (1987).
14. R.M. Welch, K.S. Kuo, B.A. Wielicki, S.K. Sengupta, L. Parker, J. Appl. Meteor. **27**, 341 (1988).
15. R.F. Cahalan, J.H. Joseph, Mon. Wea. Rev. **117**, 261 (1989).
16. G. Sèze, L. Smith, in *Proc. Seventh Conf. on Atmospheric Radiation, Amer. Meteor. Soc., San Francisco, CA* (1990), p. 47.
17. A. Davis, S. Lovejoy, D. Schertzer, in *Scaling, Fractals and Nonlinear Variability in Geophysics*, edited by S. Lovejoy, D. Schertzer (Kluwer, Dordrecht, 1991), p. 303.
18. Y. Tessier, S. Lovejoy, D. Schertzer, J. Appl. Meteor. **32**, 223 (1993).
19. A. Davis, A. Marshak, W.J. Wiscombe, R.F. Cahalan, J. Geophys. Res. **99**, 8055 (1994).
20. L.M. Romanova, Izv. Acad. Sci. USSR Atmos. Oceanic Phys. **11**, 509 (1975).
21. H.W. Baker, J.A. Davies, Remote Sens. Environ. **42**, 51 (1992).
22. A. Davis, Ph.D. thesis, McGill University, Montreal, 1992.
23. R.F. Cahalan, W. Ridgway, W.J. Wiscombe, T.L. Bell, J.B. Snider, J. Atmos. Sci **51**, 2434 (1994).
24. R.D. Cess, M.H. Zhang, Y. Zhou, X. Jing, V. Dvortsov, J. Geophys. Res. **101**, 23299 (1996).
25. A. Davis, A. Marshak, R.F. Cahalan, W.J. Wiscombe, J. Atmos. Sci. **54**, 241 (1997).
26. W.D. King, C.T. Maher, G.A. Hepburn, J. Appl. Meteor. **20**, 195 (1981).
27. C. Duroure, B. Guillemet, Atm. Res. **25**, 331 (1990).
28. B. Baker, J. Atmos. Sci. **49**, 387 (1992).
29. S.P. Malinowski, I. Zawadski, J. Atmos. Sci. **50**, 5 (1993).
30. A.V. Korolev, I.P. Mazin, J. Appl. Meteor. **32**, 760 (1993).
31. S.P. Malinowski, M.Y. Leclerc, D.G. Baumgardner, J. Atmos. Sci. **51**, 397 (1994).
32. A. Davis, A. Marshak, W.J. Wiscombe, R.F. Cahalan, J. Atmos. Sci. **53**, 1538 (1996).
33. A. Marshak, A. Davis, W.J. Wiscombe, R.F. Cahalan, J. Atmos. Sci. **54**, 1423 (1997).
34. S. Cox, D. McDougal, D. Randall, R. Schiffer, Bull. Amer. Meteor. Soc. **68**, 114 (1987).
35. B.A. Albrecht, C.S. Bretherton, D. Jonhson, W.H. Schubert, A.S. Frisch, Bull. Amer. Meteor. Soc. **76**, 889 (1995).
36. R. Boers, J.B. Jensen, P.B. Krummel, H. Gerber, Quart. J. Roy. Meteor. Soc. **122**, 1307 (1996).
37. R.F. Cahalan, J.B. Snider, Remote Sens. Environ. **28**, 95 (1989).
38. S. Lovejoy, D. Schertzer, P. Silas, Y. Tessier, D. Lavallée, Ann. Geophysicae **11**, 119 (1993).
39. S.M. Gollmer, M. Harshvardan, R.F. Cahalan, J.S. Snider, J. Atmos. Sci. **52**, 3013 (1995).
40. W.J. Wiscombe, A. Davis, A. Marshak, R.F. Cahalan, in *Proc. of the Fourth Atmospheric Radiation Measurement (ARM) Science Team Meeting, Charleston, U.S. Dept. of Energy* (1995), p. 11.
41. A. Davis, A. Marshak, H. Gerber, W.J. Wiscombe, J. Geophys. Res. (1998), to appear.
42. B.B. Mandelbrot, *Fractals: Form, Chance and Dimensions* (Freeman, San Francisco, 1977); *The Fractal Geometry of Nature* (Freeman, San Francisco, 1982).
43. S. Corssin, J. Appl. Phys. **22**, 469 (1951).
44. A. Obukhov, Izv. Akad. Naut. SSSR, Ser. Geogr. I. Geofiz. **13**, 55 (1949).
45. R.H. Kraichnan, Phys. Fluids **10**, 1417 (1967).
46. A. Arnéodo, N. Decoster, S.G. Roux, Eur. Phys. J. B **15**, 567 (2000).
47. D. Schertzer, S. Lovejoy, in *Turbulence and Chaotic Phenomena in Fluids*, edited by T. Tatsumi (North-Holland, Amsterdam, 1984), p. 505.
48. D. Schertzer, S. Lovejoy, Phys. Chem. Hyd. J. **6**, 623 (1985).
49. D. Schertzer, S. Lovejoy, J. Geophys. Res. **92**, 9693 (1987).
50. D. Schertzer, S. Lovejoy, in *Fractals: Their Physical Origin and Properties*, edited by L. Pietronero (Plenum, New York, 1989), p. 49.
51. J. Wilson, D. Schertzer, S. Lovejoy, in *Scaling, Fractals and Nonlinear Variability in Geophysics*, edited by D. Schertzer, S. Lovejoy (Kluwer, Dordrecht, 1991), p. 185.
52. D. Schertzer, S. Lovejoy, in reference [7], p. 11.
53. S. Lovejoy, D. Schertzer, in reference [7], p. 102.
54. D. Schertzer, S. Lovejoy, F. Schmitt, Y. Ghigisinskaya, D. Marsan, Fractals **5**, 427 (1997).
55. A. Davis, A. Marshak, W.J. Wiscombe, R.F. Cahalan, *Proc. of the 2nd Workshop on Nonstationary Random Processes and Their Applications* (1995), preprint.
56. N. Decoster, S.G. Roux, A. Arnéodo, Eur. Phys. J. B **15**, 739 (2000).
57. J. Arrault, Ph.D. thesis, Univ. of Bordeaux I, 1995.
58. J. Arrault, A. Arnéodo, A. Davis, A. Marshak, Phys. Rev. Lett. **79**, 75 (1997).
59. J.F. Muzy, E. Bacry, A. Arnéodo, Phys. Rev. Lett. **67**, 3515 (1991).
60. J.F. Muzy, E. Bacry, A. Arnéodo, Phys. Rev. E **47**, 875 (1993).
61. J.F. Muzy, E. Bacry, A. Arnéodo, Int. J. of Bifurcation and Chaos **4**, 245 (1994).
62. A. Arnéodo, E. Bacry, J.F. Muzy, Physica A **213**, 232 (1995).
63. K. Stamnes, S.-C. Tsay, W.J. Wiscombe, K. Jayaweera, Appl. Opt. **27**, 2502 (1988).
64. R.F. Cahalan, W. Ridgway, W.J. Wiscombe, S. Gollmer, M. Harshvardan, J. Atmos. Sci **51**, 3776 (1994).
65. A. Marshak, A. Davis, W.J. Wiscombe, R.F. Cahalan, J. Geophys. Res. **100**, 26247 (1995).
66. M. Tiedke, Mon. Wea. Res. **124**, 745 (1996).
67. A.N. Kolmogorov, J. Fluid Mech. **13**, 82 (1962).
68. A.M. Obukhov, J. Fluid Mech. **13**, 77 (1962).
69. B.B. Mandelbrot, J. Fluid Mech. **62**, 331 (1974).
70. R. Benzi, G. Paladin, G. Parisi, A. Vulpiani, J. Phys. A **17**, 3521 (1984).

71. C. Meneveau, K.R. Sreenivasan, Phys. Rev. Lett. **59**, 1424 (1987).
72. S. Kida, J. Phys. Soc. Jpn. **60**, 5 (1990).
73. C. Meneveau, K.R. Sreenivasan, J. Fluid. Mech. **224**, 429 (1991).
74. H.G.E. Hentschel, Phys. Rev. E **50**, 243 (1994).
75. E.A. Novikov, Phys. Fluids A **2**, 814 (1990); Phys. Rev. E **50**, 3303 (1995).
76. Z.S. She, E.C. Waymire, Phys. Rev. Lett. **74**, 262 (1995).
77. B. Dubrulle, Phys. Rev. Lett. **73**, 959 (1994); J. Phys. II France **6**, 1825 (1996).
78. B. Castaing, B. Dubrulle, J. Phys. II France **5**, 895 (1995).
79. A.L. Barabási, T. Vicsek, Phys. Rev. A **44**, 2730 (1991).
80. E. Bacry, J.F. Muzy, A. Arnéodo, J. Stat. Phys. **70**, 635 (1993).
81. R. Benzi, L. Biferale, A. Crisanti, G. Paladin, M. Vergassola, A. Vulpiani, Physica D **65**, 352 (1993).
82. A. Juneja, D.P. Lathrop, K.R. Sreenivasan, G. Stolovitzky, Phys. Rev. E **49**, 5179 (1994).
83. A. Davis, A. Marshak, W.J. Wiscombe, R.F. Cahalan, in *Topics in Nonstationary Analysis*, edited by G. Treviño *et al.* (World Scientific, Singapore, 1996), p. 97.
84. R.F. Cahalan, M. Nestler, W. Ridgway, W.J. Wiscombe, T.L. Bell, in *Proc. of the 4th International Meeting on Statistical Climatology*, edited by J. Sansom (New Zealand Meteorological Service, Wellington, 1990), p. 28.
85. A. Marshak, A. Davis, R.F. Cahalan, W.J. Wiscombe, Phys. Rev. E **49**, 55 (1994).
86. A. Arnéodo, N. Decoster, S.G. Roux, Phys. Rev. Lett. **83**, 1255 (1999).
87. M. Harshvardan, B.A. Wielicki, K.M. Ginger, J. of Climate **7**, 1987 (1994).
88. A. Davis, S. Lovejoy, D. Schertzer, SPIE Proc. **1558**, 37 (1991).
89. A. Marshak, A. Davis, W.J. Wiscombe, G. Titov, Remote Sens. Environ. **52**, 72 (1995).
90. F. Argoul, A. Arnéodo, J. Elezgaray, G. Grasseau, R. Murenzi, Phys. Lett. A **135**, 327 (1989); Phys. Rev. A **41**, 5537 (1990).
91. A. Arnéodo, F. Argoul, E. Bacry, J. Elezgaray, J.F. Muzy, *Ondelettes, Multifractales et Turbulences: de l'ADN aux croissances cristallines* (Diderot Éditeur, Art et Sciences, Paris, 1995).
92. A. Arnéodo, in *Wavelets: Theory and Applications*, edited by G. Erlebacher, M.Y. Hussaini, L.M. Jameson (Oxford Univ. Press, Oxford, 1996), p. 349.
93. R.G. Giovanelli, Aust. J. Phys. **12**, 164 (1959).
94. G.L. Stephens, J. Quant. Spectrosc. Radiat. Transfer **36**, 51 (1986).
95. K.F. Evans, J. Atmos. Sci. **50**, 3111 (1993).
96. S. Lovejoy, A. Davis *et al.*, J. Geophys. Res. D **95**, 11699 (1990).
97. G. Falkovich, Phys. Fluids **6**, 1411 (1994).
98. S. Grossmann, D. Lohse, Phys. Rev. E **50**, 2784 (1994).
99. D. Lohse, A. Müeller-Groeling, Phys. Rev. Lett. **74**, 1747 (1995).
100. E. Bacry, A. Arnéodo, U. Frisch, Y. Gagne, E. Hopfinger, in *Turbulence and Coherent Structures*, edited by M. Lesieur, O. Metais (Kluwer, Dordrecht, 1991), p. 203.
101. S.G. Roux, J.F. Muzy, A. Arnéodo, Eur. Phys. J. B **8**, 301 (1999).
102. S.G. Roux, Ph.D. thesis, University of Aix-Marseille II, 1996.
103. S. Douady, Y. Couder, M.E. Brachet, Phys. Rev. Lett. **67**, 983 (1991).
104. O. Cadot, S. Douady, Y. Couder, Phys. Fluids **7**, 630 (1995).
105. O. Cadot, Ph.D. thesis, University of Paris VII, 1995.
106. S. Fauve, C. Laroche, B. Castaing, J. Phys. II France **3**, 271 (1993).
107. P. Abry, S. Fauve, P. Flandrin, C. Laroche, J. Phys. II France **4**, 725 (1994).
108. P. Abry, Ph.D. thesis, University of Lyon I, 1994.
109. P. Chainais, P. Abry, J.F. Pinton, Phys. Fluids **11**, 3524 (1999).
110. B. Castaing, Y. Gagne, E.J. Hopfinger, Physica D **46**, 177 (1990).
111. A. Arnéodo, J.F. Muzy, S.G. Roux, J. Phys. II France **7**, 363 (1997).
112. A. Arnéodo, S. Manneville, J.F. Muzy, Eur. Phys. J. B **1**, 129 (1998).
113. A. Arnéodo, E. Bacry, J.F. Muzy, J. Math. Phys **39**, 4142 (1998).
114. A. Arnéodo, E. Bacry, S. Manneville, J.F. Muzy, Phys. Rev. Lett. **80**, 708 (1998).
115. A. Arnéodo, J.F. Muzy, D. Sornette, Eur. Phys. J. B **2**, 277 (1998).
116. A. Arnéodo, S. Manneville, J.F. Muzy, S.G. Roux, Phil. Trans. R. Soc. London A **357**, 2415 (1999).
117. A. Arnéodo, S. Manneville, J.F. Muzy, S.G. Roux, Appl. Computat. Harmonic Analysis **6**, 374 (1999).
118. A.N. Kolmogorov, C. R. Acad. Sci. USSR **30**, 301 (1941).
119. G. Ruiz-Chavarria, C. Baudet, S. Ciliberto, Physica D **99**, 369 (1996).
120. C.H. Meong, W.R. Cotton, C. Bretherton, A. Chlond, M. Khairoutdinov, S. Krueger, W.S. Lewellen, M.K. McVean, J.R.M. Pasquier, H.A. Rand, A.P. Siebesma, B. Stevens, R.I. Sykes, Bull. Am. Meteor. Soc. **77**, 261 (1996).